Energy 213 (2020) 118761

Contents lists available at ScienceDirect

Energy

journal homepage: www.elsevier.com/locate/energy

Hybrid thermal performance enhancement of a circular latent heat storage system by utilizing partially filled copper foam and Cu/GO nano-additives

Seyed Mohsen Hashem Zadeh [a], S.A.M. Mehryan [b], Mohammad Ghalambaz [c, d, *], Maryam Ghodrat [e], John Young [e], Ali Chamkha [f, g]

[a] *Department of Mechanical Engineering, Shahid Chamran University of Ahvaz, Iran*
[b] *Young Researchers and Elite Club, Ahvaz Branch, Islamic Azad University, Ahvaz, Iran*
[c] *Metamaterials for Mechanical, Biomechanical and Multiphysical Applications Research Group, Ton Duc Thang University, Ho Chi Minh City, Vietnam*
[d] *Faculty of Applied Sciences, Ton Duc Thang University, Ho Chi Minh City, Vietnam*
[e] *School of Engineering and Information Technology, University of New South Wales Canberra, Canberra, 2610 ACT, Australia*
[f] *Institute of Research and Development, Duy Tan University, Da Nang 550000, Vietnam*
[g] *Institute of Theoretical and Applied Research (ITAR), Duy Tan University, Hanoi 100000, Vietnam*

ARTICLE INFO

Article history:
Received 12 June 2020
Received in revised form
30 July 2020
Accepted 28 August 2020
Available online 7 September 2020

Keywords:
Latent heat thermal energy storage
Hybrid heat transfer enhancement
Metal foam-PCM composite
Nano-enhanced PCM
Partial porous media

ABSTRACT

Low thermal response of latent heat thermal energy storage (LHTES) systems has been their main barrier in large-scale applications and commercialization. Amongst all proposed techniques, the incorporation of metal foam appears to be more promising owing to the notable thermal conductivity and high ratio of surface-area-to-volume. Nonetheless, metal foams augment the thermal response of the LHTES systems at the expense of reducing their thermal capacity and weakening natural convection. The principal aim of the present study is to numerically assess the capability of hybrid heat transfer enhancement of an LHTES through a combination of partial metal foam and nano-additives. Capric acid is considered as the phase change substance in a circular-shape thermal energy storage unit with a two-pass heat pipe. A combination of Copper foam and Cu/GO nano-additives is analyzed as the hybrid enhancement approach. The outcomes show that the combination of partial copper foam with Cu/GO nano-additives is more effective than each enhancement technique separately. Moreover, the results reveal that the charging power of the LHTES can be enhanced to about four times higher than the case of pure PCM at the cost of only a 3% reduction of the thermal storage's capacity.

1. Introduction

Owing to increasing population growth, technological progress, and also life quality improvement, energy consumption has increased considerably over the last decades, resulting in a global energy crisis and environmental pollution. Hence, sustainable energy production (such as solar radiation and ocean waves) and waste heat recovery from industrial sectors have been proposed to overcome these issues. Nonetheless, intermittency and unsteady nature of these approaches need to be tackled by employing the so-called Thermal Energy Storage (TES) systems. TES systems can store the corresponding energy and discharge it whenever needed and, thus, they play a key role in the development of renewable energies and industrial waste heat recovery systems. According to the mechanism of storing energy, TES systems are categorized into three types of sensible, latent, and thermo-chemical thermal energy storage. Owing to their much higher energy storage density and also narrow temperature interval during the charging/discharging process, LHTES systems have gained much interest and been promising options for saving energy. In an LHTES system, thermal energy is stored (or released) during phase transition (mainly solid to liquid and vice versa) of a substance called Phase Change Material (PCM) with a characteristic of very high latent heat [1].

Slow thermal response (low thermal conductivity) of all types of

---

* Corresponding author. Ton Duc Thang University, Ho Chi Minh City, Vietnam.
E-mail addresses: mohsen.hashemzadeh@gmail.com (S.M. Hashem Zadeh), mohammad.ghalambaz@tdtu.edu.vn (M. Ghalambaz), alichamkha@duytan.edu.vn (A. Chamkha).

https://doi.org/10.1016/j.energy.2020.118761
0360-5442/© 2020 Elsevier Ltd. All rights reserved.

Nomenclature

Latin symbols

A_{mush}	mushy zone constant
$a(T)$	Porosity function
c_p	Specific heat of the suspension in constant pressure
d_p	Pore size
d_l	Ligament diameter
g	Gravity acceleration
h_{sf}	Latent heat of the PCM
K	Permeability of the porous media (copper foam)
MVF	Melted volume fraction
p	Pressure field
r	Radius
r_h	Radius of the heat pipe
r_p	Radius of the porous zone
r_s	Radius of the storage
t	time
T	Temperature
T_{fu}	Fusion temperature
U	Velocity vector
u	x-component of the velocity
v	y-component of the velocity
x	x-Cartesian coordinate
y	y-Cartesian coordinate

Greek symbols

λ	Thermal conductivity coefficient
μ	Dynamic viscosity
β	Coefficient of thermal expansion
δ	Porosity of the porous media (copper foam)
ξ	Pore density
σ	Melt volume fraction
ρ	Density
ω	Volume fraction of nano-additives
χ	Parameter defined in Eq. 13b
η	Angle of the heat pipe with horizon

Subscript

cz	Clear zone
Cu	Cu nano-additive
GO	GO nano-additive
pz	Porous zone
pm	Porous media (copper foam)
eff	Effective value
s	Storage, solid
NeP	Nano-enhanced PCM
k	Domain indicatior (porous or clear)
na	Nano-additives
sm	Solid matrix of the porous medium
PCM	Phase change material
l	Liquid

PCMs is considered to be their main drawback that significantly slows down their charging and discharging process and restricts their large-scale utilization. To overcome this barrier, extensive surveys have been carried out that can be grouped as: (1) improving uniformity of heat transfer process, (2) extending surface area of heat transfer, and (3) enhancing PCMs thermal conductivity [1]. Concerning the first group, i.e., increasing uniformity of heat transfer process, thermodynamic optimization, and employing multiple PCMs with different fusion point (cascaded LHTES systems) are the most prominent approaches [2,3].

To increase the surface area of heat transfer in LHTES, namely the second group, two commonly used techniques are finned surfaces and also encapsulation. Finned tubes are mainly used in shell and tube LHTES systems. Despite the advantages of finned surface, such as low cost, easy implementation, and effectiveness, assembling fins to the TES systems increases their weight and also reduces their thermal storage capacity (because of the space occupied by fins) [4]. Macro- and micro-encapsulation is another promising technique that can be used to increase the surface area of heat transfer in LHTES systems. Encapsulated phase change materials consist of a PCM as core and a rigid shell that surrounds the core. In addition to increasing the surface area of heat transfer, encapsulation has numerous advantages, such as preventing PCM leakage from the structure during the phase transition, reducing the interference with surrounding, and retarding the volume change of PCMs [5–7]. For this purpose, encapsulated PCMs are assembled in a tank, and a heat transfer fluid (HTF) is passed through the gaps between capsules. The overall rate of heat transfer and also melting and solidification rates of PCMs boost as the encapsulation process downsized to micro- and nanoscales [8,9]. However, micro- and nano-encapsulation techniques suffer from some demerits such as highly expensive processes, the chance of supercooling effect, and also interrupting natural convection during the solidification process [10]. The thermophysical properties of nanomaterials [11] and nanofluids [12,13] have been reviewed recently. These reviews provide a comprehensive outline of the modeling and advantage of nano-enhanced materials.

Finally, with regards to the last group, i.e., enhancing the thermal conductivity of PCMs, two general approaches, namely employing nano-additives and highly conductive porous medium, are used to form Composite Phase Change Materials (CPCMs). Different nanomaterials such as MWCNT, graphite, graphene (suitable for both low and high-temperature PCMs), metal, and metal oxides (pertinent for low-temperature PCMs) are commonly used for preparing nano-additive CPCM [1,14–16]. Lohrasbi et al. [17] numerically analyzed the discharging process of a fin-assisted LHTES enhanced with copper nanoparticles. They used a Y-shaped aluminum fin and showed that by increasing fin length, due to the heat diffusion, the solidification time reduces up to 32%. Moreover, they analyzed the impact of copper nanoparticles on the solidification of the LHTES. They revealed that the solidification time could be reduced by around 17% when 5% volume fraction of copper nanoparticle is added to the base PCM.

Sheikholeslami and Mahian [18] investigated the phase change heat transfer of nano-enhanced PCMs during the solidification process in an enclosure using Finite Element Method. They reported that dispersing 4% CuO nanoparticles could reduce the solidification time up to 14%. Lin and Al-Kayiem [19] dispersed 20 nm Cu nanoparticles into paraffin wax to synthesis Cu–PCM nanocomposites. It was found that the thermal conductivity of the nanocomposite can be augmented to around 50% for 2% weight of Cu-nanoparticles. Furthermore, they found that the latent heat and fusion point of the nanocomposite of Cu-PCM reduces because of the agglomeration of the copper nanoparticles. Barhemmati-Rajab and Zhao [20] reported 71.9% increase in the conductivity of the calcium chloride hexahydrate ($CaCl_2.6H_2O$) as the PCM by dispersing 0.5 wt% boron nitride. Yang et al. [65] reviewed the thermophysical properties and various applications of the nano-enhanced PCMs in thermal energy storage (TES), photovoltaic thermal (PVT), solar still (SS), thermal control unit (TCU). It was stated that the incorporation of nano-additives enhance the melting/solidification rates of PCMs in all of the their applications.

Owing to their high thermal conductivity, metal foam-PCM composites are widely used in LHTES systems. The most commonly used materials, copper foam, aluminum foam, and nickel foam, have shown a substantial impact on the overall thermal conductivity of the CPCMs and their melting (charging) time [21]. A wide range of porosities and pore densities are available for foams. Extensive experimental and numerical tests have been carried out to assess the thermal performance enhancement of the metal foam-PCM composites. For example, Xiao et al. [22] studied two metal foam-PCMs comprising paraffin/nickel foam and paraffin/copper foam composite phase change materials in an LHTES. They found that compared to the case of pure paraffin, the thermal conductivity of the CPCM could be elevated up to three times for paraffin/nickel composite PCMs and fifteen times for paraffin/copper composite PCMs. In another study, Mancin et al. [23] analyzed the solid to the liquid phase transition process for three different paraffin-waxes embedded in copper foam with a porosity of 0.95. They found that metallic foam can substantially enhance the rate of heat transfer in passive approaches. Mehryan et al. [24] numerically analyzed the phase transition process of a non-Newtonian PCM in a porous coaxial pipe filled with aluminum foam with a porosity of 0.9. They found that the melting rate intensifies as the power-law index of the PCM decreases. Moreover, with decreasing the Stefan number, the melting time reduces significantly. Ghalambaz and Zhang [25] numerically surveyed the conjugate phase change process in a heat sink filled with paraffin wax-nickel foam composite under a pulse heat load. It was found that the utilization of nickel foam in the heatsink could improve the rate of heat transfer at the hot surface, especially when external cooling power is low. Ghahremannezhad et al. [66] studied impact of non-homogeneous porous copper foam on phase change behavior of paraffin in a LHTES with rectangular storage. It was found that location of heat source and also direction of gradient metal foam can affect the charging time of the storage and for the case of left-heated storage, the lowest charging time can be obtained when a porous foam with positive gradient porosity foam in xdirection is utilized.

Recently, hybrid approaches (i.e., combinations of two or more techniques) for thermal performance augmentation of the LHTES system have been proposed [26,27]. In fact, it is argued that the level of enhancement is not adequate for single techniques and LHTES systems still suffer from the low thermal response. Xie et al. [28] conducted experimental research to assess the thermal performance improvement of metallic foam and fins in an LHTES. They used eicosane as the phase change substance and copper foam with 96% porosity and showed that the utilization of fins could increase the melting rate of the TES system up to 2.7 times higher than the case without fins. Zhang et al. [29] analyzed the improvement level of a combination of finned surface and copper foam in a heat pipe latent heat thermal energy storage system. They revealed that the combination results in better performance than sole fins or copper foam. In addition, it was found by exergy analysis that as the total volume fraction of both fins and copper foam increases, the rate of phase transition intensifies; however, the role of natural convection retards reasonably. Similar researches on a combination of fins and metal foams have been conducted by Feng et al. [30], Srivatsa et al. [31], and Zhang et al. [32] (for heat pipe-based fins). Also, combinations of fins and nanoparticles [33–35] and a combination of nano-additives and metallic foams [36–40] for thermal enhancement of thermal storage systems have been investigated by some researchers. Latterly, in an excellent work, Mahdi et al. [26] reviewed the recent progress on hybrid thermal enhancement approaches of LHTES systems. It was concluded that hybrid utilization of nanoparticle with fins or metal foams is more efficient than the sole use of nanoparticles. The idea of a combination of techniques for thermal response enhancement of LHTES is yet in need of further assessment since it might not be beneficial for all techniques to be merged. For example, Buonomo et al. [39] numerically studied the phase transition process of nanocomposite PCM saturated in a metallic foam. It was found that the melting rate of the PCM enhances when the porosity of the metallic foam reduces. Moreover, they revealed that the presence of nanoparticles increases the melting rate; however, high values of nanoparticles volume fraction could suppress natural convection as it raises the viscosity of liquid composite PCM.

As could be concluded from the above discussion, the presence of metal foams can extremely enhance the thermal performance of the LHTES system. Nonetheless, the latent heat and melting temperature of PCMs are affected by the utilization of composite PCMs. In addition to this, their manufacturing technology is complicated and costly. Most importantly, the natural convection heat transfer is weakened, which is considered as the main disadvantage of metallic foam-PCM composites. Nevertheless, to the best of authors' knowledge, very limited research can be found that addressed the mentioned drawbacks of metal foam-PCM composites. Metal foams augment the heat diffusion throughout the PCM domain at the expense of reducing natural convection and less PCM volume (occupied by the metal foam). Indeed, because of the buoyancy force, phase change proceeds faster on the upper portion of the enclosures comparing to the lower parts. Hence, it could be more efficient to implement a partial porous medium in the lower parts of the storage. This approach can uniform the melting process with the minimum area occupied by the porous medium. In other words, this concept can reduce the charging time of LHTES systems without a notable reduction in their thermal capacity. Xu et al. [67] numerically surveyed the phase change performance of PCMs in a horizontal concentric-tube LHTES system. They assessed the performance of embedding porous foams with four different configurations (none porous insert, full porous insert, lower and upper porous inserts). It was found that position of the porous foam can meaningfully affect the melting rate. In fact, the melting rate is higher when the porous foam is installed on the lower portion of the storage. Joshi and Rathod [68] analyzed the melting front of a pure PCM in a square cavity and found that at the top half, the propagation of the melting front is faster, and hence, they investigated the influence of partial metal foam installation at the bottom of the cavity for two different configurations. It was found that with such structural modification, the melting time could be reduced up to 40%. In another study, Joshi and Rathod [69] numerically studied the thermal enhancement of partial metal foam in a square cavity. The height of the porous foam and its porosity was analyzed as influential parameters and was found that it is more efficient to employ the metal foam on lower part of the cavity. Moreover, it was found that when the filling height is 0.75 of cavity, the melting time is almost the same as the case of full porous foam installation. Besides, it was shown that porous foams with higher porosities should be chosen to minimize the reduction of the LHTES capacity.

The present study aims to evaluate how efficient could be the hybrid incorporation of partial metal foam and nano-additives in a circular latent heat thermal energy storage with a two-pass heat pipe. Moreover, the trade-off between the heat capacity of LHTES and its charging power will be addressed. To study the impact of the geometrical features of the storage, the angle of heat pipes with the horizon, as well as the porosity and eccentricity of the partial metal foam, are examined. Moreover, to assess the potential of nano-additives on the thermal enhancement of the LHTES system, two nano-particles of Cu and GO are considered. The effects of the mentioned parameters are evaluated in terms of isothermal and streamline contours, thermal capacity, and the average charging power. Finally, for a constant volume of PCM, the efficiency of combinations of partial metal foam and nano-additives are presented and discussed.

2. Mathematical model

The configuration of the thermal energy storage unit employed in this study is depicted in Fig. 1. The heat pipe located in the unit is surrounded by an eccentric porous annulus with porosity δ and permeability K. The eccentricity of the porous annulus with respect to the centerline of the heat pipe is e. The heat pipe is made of a high thermally conductive material with a low thickness. Consequently, the temperature difference between the condenser and evaporator section of the heat pipe is not high, and it can be assumed that its temperature is constant at T_h. These assumptions and reasons reduce the 3D computational domain to a 2D one. The clear and porous zones are saturated with a nano-enhanced phase change material (NePCM) of the Capric acid as the PCM and Cu/GO as the nano-additives. The employed NePCM could be prepared by using the so-called two-step method, in which, first, the Cu/GO nano-additives are produced and then, dispersed in the liquid Capric acid as PCM [70,71]. The thermophysical characteristics of the solid matrix of the porous mediums, the phase change material, and the nano-additives are tabulated in Table 1. It is worth mentioning that for each simulation, only one of the nano-additives of Cu or GO was considered. Since the nanoparticles are very fine, they can be uniformly and stably dispersed in the PCM. Due to their miniature size, they do not clog the tiny pores of the metal foam. Hence, the NEPCM liquid could be modeled as a uniform suspension with enhanced thermophysical properties, which was embedded in a metal foam. The geometrical characteristics of the 2D computational domain are illustrated in Fig. 1b in which $r_s = 40$ mm, $r_h = r_s/4$, and $r_{pm} = 4r_s/10$.

The control equations of the governing physics are as follows [43–45]:

Continuity equation:

$$\frac{\partial u}{\partial x} + \frac{\partial v}{\partial y} = 0 \tag{1}$$

x- and y-momentum equations:

$$\frac{\rho_{NeP,l}}{\delta_k^2}\left[\delta_k \frac{\partial u}{\partial t} + (\vec{U}\cdot\nabla)u\right] = -\frac{\partial p}{\partial x} + \frac{\mu_{NeP,l}}{\delta_k}\nabla^2 u + Bu \tag{2}$$

$$\frac{\rho_{NeP,l}}{\delta_k^2}\left[\delta_k \frac{\partial v}{\partial t} + (\vec{U}\cdot\nabla)v\right] = -\frac{\partial p}{\partial y} + \frac{\mu_{NeP,l}}{\delta_k}\nabla^2 v + Bv + \rho_{NeP,l}\, g\beta_{NeP,l}\left(T - T_{fu}\right) \tag{3}$$

Energy equation:

$$(\rho C_p)_k \frac{\partial T}{\partial t} + (\rho C_p)_{NeP,l}(\vec{U}\cdot\nabla)T = \lambda_k \nabla^2 T - \rho_{NeP,l} h_{sf,NeP}\delta_k \frac{\partial \sigma(T)}{\partial t} \tag{4}$$

The coefficient B in Eqs. (2) and (3) is:

$$B = -\frac{\mu_{NeP,l}}{K_k} - a(T) \tag{5}$$

where the first term in the right hand side of Eq. (4) is based on the Darcy-Brinkman model. Moreover, $a(T)$, is the porosity function and defined as the following:

$$a(T) = A_{mush}\frac{(1-\sigma(T))^2}{\sigma(T)^3 + \varsigma} \tag{6a}$$

in which,

$$\sigma(T) = \begin{cases} 0 & T < T_{fu} - \dfrac{\Delta T}{2} \\ \dfrac{T - T_{fu}}{\Delta T} + \dfrac{1}{2} & T_{fu} - \dfrac{\Delta T}{2} < T < T_{fu} + \dfrac{\Delta T}{2} \\ 1 & T > T_{fu} + \dfrac{\Delta T}{2} \end{cases} \tag{6b}$$

spatial functions δ_k (porosity) and K_k(permeability) are defined

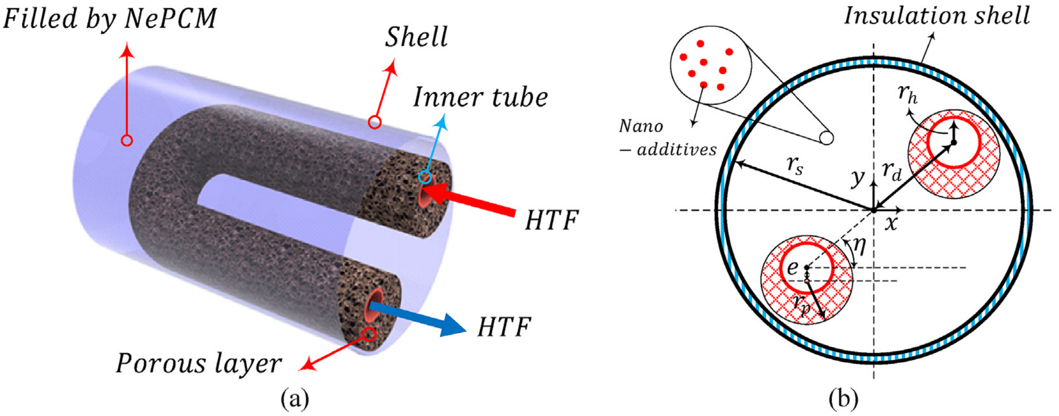

(a) (b)

Fig. 1. (a) Configuration of the thermal energy storage unit and (b) cross-section of the unit.

Table 1
Thermophysical properties of the capric acid, metal foam, and the nano-additives [41,42].

Properties	Capric acid	Copper foam	Cu nano-additives	GO nano-additives
Density ($kg\ m^{-3}$)	Solid: 1018 Liquid: 888	8900	8933	1800
Specific heat ($kJ\ kg^{-1}\ K^{-1}$)	Solid: 1900 Liquid: 2400	0.386	0.385	0.717
Thermal expansion coefficient (K^{-1})	1×10^{-3}	NA	1.67×10^{-5}	28.4×10^{-5}
Fusion temperature (°C)	32	NA	NA	NA
Thermal conductivity ($Wm^{-1}\ K^{-1}$)	Solid: 0.372 Liquid: 0.153	380	401	5000
Latent heat ($kJ\ kg^{-1}$)	152.7	NA	NA	NA
Kinematic viscosity ($m^2\ s^{-1}$)	3×10^{-6}	NA	NA	NA

based on the clear and porous zones as the following:

$$\delta_k = \begin{cases} \delta & k=1 \\ 1 & k=2 \end{cases}, \quad K_k = \begin{cases} K & k=1 \\ \infty & k=2 \end{cases} \tag{7}$$

The permeability of the metal foam is given as [27,46,47]:

$$K = d_p^2 \, \frac{73 \times 10^{-5}}{(1-\delta)^{0.224}} \left(\frac{d_l}{d_p}\right)^{-1.11} \tag{8a}$$

$$\frac{d_l}{d_p} = 1.18 \left(\frac{1-\delta}{3\pi}\right)^{0.5} \left[1 - \exp(-(1-\delta)/0.04)\right]^{-1} \tag{8b}$$

in which,

$$d_p = 254 \times 10^{-4} \xi^{-1} \ (PPI) \tag{8c}$$

The heat capacity in Eq. (4) is defined as:

$$(\rho C_p)_k = \begin{cases} (\rho C_p)_{pm,eff} & k=1 \\ (\rho C_p)_{NeP,l} & k=2 \end{cases} \tag{9}$$

in which,

$$(\rho C_p)_{pm,eff} = \sigma(T)(\rho C_p)_{pm,eff,l} + (1-\sigma(T))(\rho C_p)_{pm,eff,s} \tag{10a}$$

$$(\rho C_p)_{pm,eff,i} = (1-\delta_k)(\rho C_p)_{sm} + \delta_k (\rho C_p)_{NeP,i} \tag{10b}$$

Subscript i denotes both the fluid and solid phases of the NePCM. λ_k of the energy equation is defined as the following:

$$\lambda_k = \begin{cases} \lambda_{pm,eff} & k=1 \\ \lambda_{NeP} & k=2 \end{cases} \tag{11}$$

The thermal conductivity of the porous medium and the NePCM are functions of the melt volume fraction as the following:

$$\lambda_{pm,eff} = \sigma(T)\lambda_{pm,eff,l} + (1-\sigma(T))\lambda_{pm,eff,s} \tag{12a}$$

$$\lambda_{NeP} = \sigma(T)\lambda_{NeP,l} + (1-\sigma(T))\lambda_{NeP,s} \tag{12b}$$

There are various relations for evaluating the effective thermal conductivity of porous media and metal foams. Many of the relations are discussed in the comprehensive review study of Ranut [48]. The most commonly used equation is the following relation [49,50]:

$$\lambda_{pm,eff,i} = \frac{\left[\lambda_{NeP,i} + \pi\left(\sqrt{\chi} - \chi\right)\Delta\lambda\right]\left[\lambda_{NeP,i} + (\chi\pi)\Delta\lambda\right]}{\lambda_{NeP,i} + \left[\frac{4}{3}\sqrt{\chi}(1-\delta) + \pi\sqrt{\chi} - (1-\delta)\right]\Delta\lambda} \tag{13a}$$

in which,

$$\chi = \frac{1-\delta}{3\pi}, \ \Delta\lambda = \lambda_{sm} - \lambda_{NeP,i} \tag{13b}$$

The thermo-physical characteristic of the NePCM

Dispersion of nano-additives impacts all the thermo-physical characteristics of PCMs. Nonetheless, to accurately simulate the obtained NePCM, effective thermal conductivity and viscosity of NePCMs are the principal properties and need to be specially treated. In fully melted condition, NePCMs behaves as a nanofluid. The main different with simple nanofluid is that the NePCMs can also be found in solid and mushy (semi-solid) states, and hence, NePCMs exhibit different thermal and rheological behaviors as their temperatures varies. The presence of nanoparticles in the base liquid PCM can be addressed using the so-called single-phase approaches of nanofluids. In these models, the Brinkman and Maxwell models are employed to estimate the viscosity and the effective thermal conductivity of the liquid NePCM [63]. It is worth mentioning that the nanoparticles are assumed to have spherical shape and the base fluid and nano-sized particles are flowing with equal velocities (no-slip boundary condition). Moreover, the predicted effective thermal conductivity and dynamic viscosity of the NePCM are reliable when the volume fraction of the nano-additives in the NePCM is less than 0.08 [64]. The density of NePCM, as a mixture of two components, is defined as:

$$\rho_{NeP} = \rho_{PCM} + \omega_{na}(\rho_{na} - \rho_{PCM}) \tag{14a}$$

$$\rho_{PCM}(T) = \rho_{PCM,l}\sigma(T) + (1-\sigma(T))\rho_{PCM,s} \tag{14b}$$

in which ω_{na} is the volume fraction of the nano-additives. The effective dynamic viscosity of the NePCM is estimated by the following relation [60,61]:

$$\mu_{NePCM,l} = \mu_{PCM,l}(1-\omega_{na})^{-2.5} \tag{15}$$

Similarity, the thermal-volume expansion coefficient is evaluated as the following:

$$\rho_{NeP,l}\beta_{NeP,l} = \rho_{PCM,l}\beta_{PCM,l} + \omega_{na}\left(\rho_{na}\beta_{na} - \rho_{PCM,l}\beta_{PCM,l}\right) \tag{16}$$

The effective thermal conductivity of the NePCM can be obtained by employing the mentioned-below equation [60,62]:

$$\frac{\lambda_{NeP,i}}{\lambda_{PCM,i}} = \frac{(\lambda_{na} + 2\lambda_{PCM,i}) - 2\omega_{na}(\lambda_{PCM,i} - \lambda_{na})}{(\lambda_{na} + 2\lambda_{PCM,i}) + \omega_{na}(\lambda_{PCM,i} - \lambda_{na})} \tag{17}$$

Furthermore, the effective heat capacity of the NePCM is:

$$\rho_{NeP}C_{p,NeP} = \rho_{PCM}C_{p,PCM} + \omega_{na}\left(\rho_{na}C_{p,na} - \rho_{PCM}C_{p,PCM}\right) \tag{18a}$$

$$\rho_{PCM}C_{p,PCM}(T) = \rho_{PCM,l}C_{p,PCM,l}\sigma(T) + (1-\sigma(T))\rho_{PCM,s}C_{p,PCM,s} \tag{18b}$$

Finally, the effective heat latent of the NePCM can be evaluated as follows:

$$\rho_{NeP,l}h_{sf,NeP} = (1-\omega_{na})\rho_{PCM,l}h_{sf,PCM} \tag{19}$$

The boundary conditions at the interface of the porous and clear regions are the continuities of the temperature and heat flux as the following:

$$T|_{cz} = T|_{pz},\ \lambda_{NeP}\frac{\partial T}{\partial n}\bigg|_{cz} = \lambda_{pm,eff}\frac{\partial T}{\partial n}\bigg|_{pz} \tag{20a}$$

Also, the mathematical form of the applied boundary conditions on the shell and the inner pipes is as the following:

$$u = v = 0,\ \frac{\partial T}{\partial n} = 0 \tag{20b}$$

$$u = v = 0,\ T = T_h \tag{20c}$$

where n is the normal direction to the surfaces. Moreover, the initial boundary condition is

$$u = v = 0,\ T = T_c \tag{21}$$

The capacity of the storage is the total energy stored in the NePCM includes the latent and sensible energy which can be formulated as follows:

$$\text{Total Capacity of the Storage} = \int_A (\rho C_p)_k (T - T_c)\, dA + \int_A \rho_{NeP,l}h_{sf,NeP}\delta_k dA \tag{22}$$

Finally, the melted volume fraction (*MVF*) is evaluated as:

$$MVF = \frac{\int_A \delta_k \chi(T) dA}{\int_A \delta_k dA} \tag{23}$$

3. Numerical method

In the present phase change problem, there are two important source terms. There is a source term in the momentum equation, which controls the velocity vector at the solid and liquid regions. The velocity source term $a(T)$ is a function of the domain temperature (T), and it approaches a very large value when the domain temperature is lower than fusion temperature, which leads to a zero velocity. The other important source term is the term of $\partial\sigma(T)/\partial t$, which corresponds to the latent heat of fusion. When the domain temperature reaches to the fusion temperature, the temperature remains constant, and this term controls the phase domain of σ. Hence, at the melting/solidification interface, there is a significant change in the momentum equation as well as in the heat equation. Thus, a high-quality mesh with high resolution is required at the phase change interface.

Moreover, due to the low thermal conductivity of PCMs and the presence of natural convection effects in the enclosure, the melting/solidification interface is a small region in the domain of the solution. The thickness of the melting/solidification region can be controlled by the fusion temperature range ΔT. A small value of ΔT result is a sharp and very thin melting/solidification interface, which is physically expected. However, a skinny layer in the domain of solution requires a very dense mesh, which, computationally, is very expensive even for a 2D domain of solution. Therefore, mesh adaptation at a region about the melting/solidification interface can capture the phase change interface with a high resolution and relatively low computational cost.

Another important aspect of the present work is the time step. Attention to the fusion source term of $\partial\sigma(T)/\partial t$shows that the phase-field σ is a function of temperature domain (T) while T is a function of space and time. Therefore, this term is susceptible to the chain of differentiation and the selected time step and the quality of the utilized mesh. However, as mentioned, a very dense grid raises the computational time while a non-dense grid requires a very small time step which again leads to high computational costs. Thus, an automatic time step is also required to balance time accuracy and mesh adaptation.

Here, a Finite Element Method (FEM) is developed to solve the governing equations of (1)-(4) along with the corresponding boundary conditions of Eq. (20) (a)-(c) and the initial condition of Eq. (21). The COMSOL Multiphysics software was used to numerically solve the governing equations. User defined codes were written for the mesh adaptation control and velocity control of the flow at the mushy interface, the solid region, and the liquid region. Following the FEM, the governing equations are written in a weak form, and the following basis set $\{\gamma_k\}_{k=1}^{N}$ is adopted to expand the $x-$ and $y-$velocity equations as well as the pressure, and the temperature equations as

$$u \approx \sum_{m=1}^{N} u_m\gamma_m(x,\ y), v \approx \sum_{m=1}^{N} v_m\gamma_m(x,\ y),\ p \approx \sum_{m=1}^{N} p_m\gamma_m(x,\ y),\ T \approx \sum_{m=1}^{N} T_m\gamma_m(x,\ y) \tag{24}$$

The temperature and pressure are expanded using linear shape functions. The adopted set of the basis functions (γ) is the same for the variables, and the adopted mesh is an unstructured mesh. Invoking the Galerkin finite element method, the governing equations can be written as a set of the residual functions at each node of the domain of solution as

$$R_i^1 \approx \sum_{m=1}^{N} u_m \int \frac{\partial \gamma_m}{\partial x}\gamma_i dxdy + \sum_{m=1}^{N} v_m \int \frac{\partial \gamma_m}{\partial y}\gamma_i dxdy \tag{25a}$$

$$\begin{aligned} R_i^2 \approx{} & \frac{\rho_{NeP,l}}{\delta_k}\sum_{m=1}^{N} u_m \int \frac{\partial \gamma_m}{\partial t}\gamma_i dxdy + \frac{\rho_{NeP,l}}{\delta_k^2}\sum_{m=1}^{N} u_m \int \left[\left(\sum_{m=1}^{N} u_m\gamma_m\right)\frac{\partial \gamma_m}{\partial x} + \left(\sum_{k=1}^{N} v_m\gamma_m\right)\frac{\partial \gamma_m}{\partial y}\right]\gamma_i dxdy \\ & + \sum_{m=1}^{N}\int\left(-\sum_{m=1}^{N} p_m\gamma_m\right)\frac{\partial \gamma_m}{\partial x}\gamma_i dxdy + \frac{\mu_{NeP,l}}{\delta_k}\sum_{m=1}^{N} u_m \int \frac{\partial \gamma_m}{\partial x}\frac{\partial \gamma_i}{\partial x} dxdy \\ & + \frac{\mu_{NeP,l}}{\delta_k}\sum_{m=1}^{N} u_m \int \left[\frac{\partial \gamma_m}{\partial y}\frac{\partial \gamma_i}{\partial y}\right] dxdy - \frac{\mu_{NeP,l}}{\delta_k}\int\left(\sum_{m=1}^{N} u_m\gamma_m\right)\gamma_i dxdy - a(T)\int\left(\sum_{m=1}^{N} u_m\gamma_m\right)\gamma_i dxdy \end{aligned} \tag{25b}$$

$$\begin{aligned} R_i^3 \approx{} & \frac{\rho_{NeP,l}}{\delta_k}\sum_{m=1}^{N} v_m \int \frac{\partial \gamma_m}{\partial t}\gamma_i dxdy + \frac{\rho_{NeP,l}}{\delta_k^2}\sum_{m=1}^{N} v_m \int \left[\left(\sum_{m=1}^{N} u_m\gamma_m\right)\frac{\partial \gamma_m}{\partial x} + \left(\sum_{k=1}^{N} v_m\gamma_m\right)\frac{\partial \gamma_m}{\partial y}\right]\gamma_i dxdy \\ & + \sum_{m=1}^{N}\int\left(-\sum_{m=1}^{N} p_m\gamma_m\right)\frac{\partial \gamma_m}{\partial y}\gamma_i dxdy + \frac{\mu_{NeP,l}}{\delta_k}\sum_{m=1}^{N} v_m \int \frac{\partial \gamma_m}{\partial x}\frac{\partial \gamma_i}{\partial x} dxdy \\ & + \frac{\mu_{NeP,l}}{\delta_k}\sum_{m=1}^{N} v_m \int \left[\frac{\partial \gamma_m}{\partial y}\frac{\partial \gamma_i}{\partial y}\right] dxdy - \frac{\mu_{NeP,l}}{\delta_k}\int\left(\sum_{m=1}^{N} v_m\gamma_m\right)\gamma_i dxdy \\ & - a(T)\int\left(\sum_{m=1}^{N} v_m\gamma_m\right)\gamma_i dxdy + \rho_{NeP,l} g \beta_{NeP,l}\left(\int\left(\sum_{m=1}^{N} T_m\gamma_m\right)\gamma_i dxdy - T_{fu}\right) \end{aligned} \tag{25c}$$

$$\begin{aligned} R_i^4 \approx{} & (\rho C_p)_k \sum_{m=1}^{N} T_m \int \frac{\partial \gamma_m}{\partial t}\gamma_i dxdy \\ & + (\rho C_p)_{NeP,l}\sum_{m=1}^{N} T_m \int \left[\left(\sum_{m=1}^{N} u_m\gamma_m\right)\frac{\partial \gamma_m}{\partial x} + \left(\sum_{m=1}^{N} v_m\gamma_m\right)\frac{\partial \gamma_m}{\partial y}\right]\gamma_m dxdy \\ & + \lambda_k \sum_{m=1}^{N} T_m \int \left[\frac{\partial \gamma_m}{\partial x}\frac{\partial \gamma_i}{\partial x} + \frac{\partial \gamma_m}{\partial y}\frac{\partial \gamma_i}{\partial y}\right] dxdy - \rho_{NeP,l} h_{sf,NeP}\delta_k \sum_{m=1}^{N}\frac{\partial \sigma(T_m)}{\partial T}\int \frac{\partial \gamma_m}{\partial t}\gamma_i dxdy \end{aligned} \tag{25d}$$

where

$$\frac{\partial \sigma(T)}{\partial T} = \begin{cases} 0 & T \le T_{fu} - \dfrac{\Delta T}{2} \\ \dfrac{1}{\Delta T} & T_{fu} - \dfrac{\Delta T}{2} < T < T_{fu} + \dfrac{\Delta T}{2} \\ 0 & T \ge T_{fu} + \dfrac{\Delta T}{2} \end{cases} \tag{26}$$

In the residual equations, the integrals are integrated using the second-order Gaussian-quadrature method. More details about the Galerkin finite element method can be found in Ref. [51,52].

A modified phase-field variable $\sigma_0$is adopted as a bound for grid adaptation where $\sigma_0 = 1$ defined the space-domain marked for mesh adaptation. It is assumed that the phase change occurs at a slightly thicker temperature range of $3\Delta T/2$ instead of ΔT. This slightly larger fusion bond leads to a wider physical domain around the melting/solidification interface, which allows a smooth mesh transient at the phase change interface. The refined mesh in the domain marked by $\sigma_0 = 1$ is five-times smaller than the regular mesh of the domain. Here, $\sigma_0$is defined as

$$\sigma_0(T) = \begin{cases} 0 & T \le T_{fu} - \dfrac{3}{2}\Delta T \\ 1 & T_{fu} - \dfrac{3}{2}\Delta T < T < T_{fu} + \dfrac{3}{2}\Delta T \\ 0 & T \ge T_{fu} + \dfrac{3}{2}\Delta T \end{cases} \tag{27}$$

Moreover, as long as the phase change interface is inside the adaptation domain, the mesh is adequate for computations. Hence, a slightly larger adaptation area around the phase change interface reduces the number of required adaptations procedures. Although

Table 2
Details of the employed grids for independency test.

Grid No.	1	2	3	4	5	6	7
Total No. of elements	4658	7898	9576	11108	13016	14318	23698
Computing time (min)	62	81	97	108	122	137	176

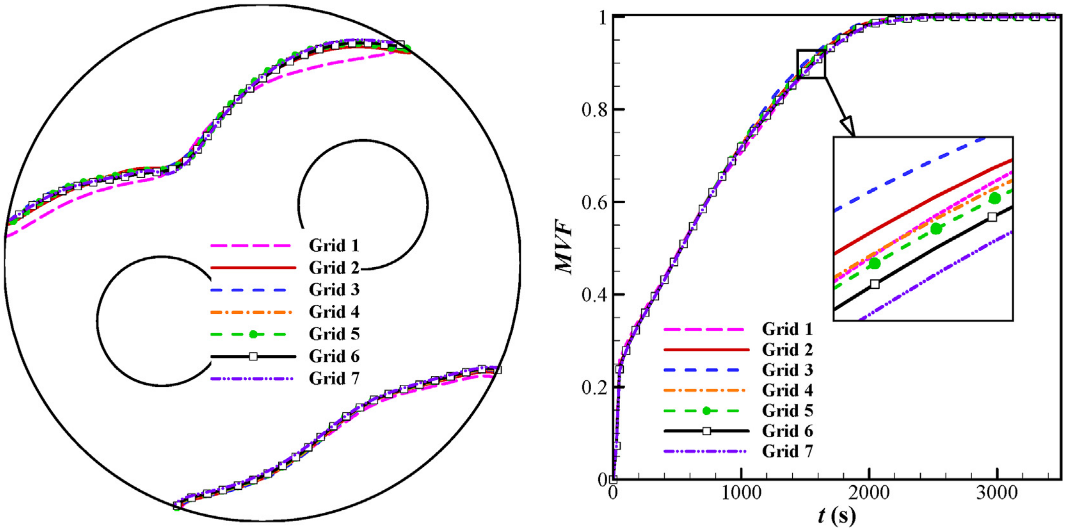

Fig. 2. Dependency of the melting interface (left) and liquid fraction of the NePCM (right) on the grid density ($\eta = \pi/6$, $\omega_{GO} = 0.04$, $\omega_{Cu} = 0.0$, $e = 0.14r_c$, $\delta = 0.8$).

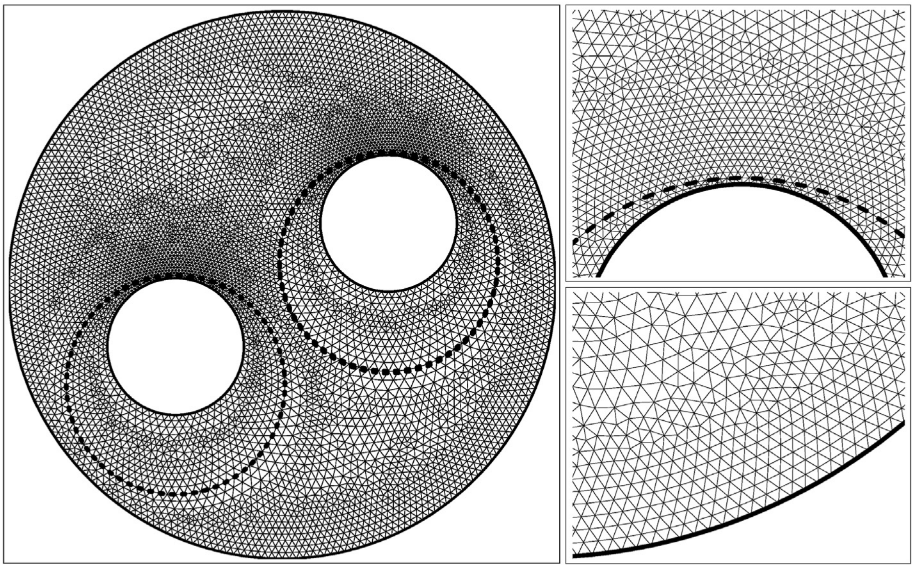

Fig. 3. The utilized gird for computations (Grid 5) at the start of simulation.

mesh adaptation in a larger domain increases the number of mesh elements and computational costs, a mesh adaptation is also an expensive computational step, which can be avoided at some intermediate time steps by adopting a slightly larger mesh-adaptation domain. Hence, the utilized approach is computationally effective.

In the present study, an automatic time step, free step Backward Differentiation Formula (BDF) is utilized to control the time steps within a variable order in the range of one and two [53]. The residual equations of Eq. (25) are iteratively solved by the Newton method utilizing a PARallel DIrect SOlver (PARDISO) solver [54–56] with a Newtonian damping factor of 0.8 and a residual error O(10^{-6}).

4. Grid study and independency test

As shown in Table 2, seven different meshes with different element numbers were used to examine the mesh independence of the results. Fig. 3 shows the non-structured grid used in this study (case 5). A dense mesh was provided, especially for the curvature region of the domain. Different element numbers were compared with respect to melting interface and liquid fraction of the NePCM vs time, for $\eta = \pi/6$, $\omega_{GO} = 0.04$, $\omega_{Cu} = 0.0$, $e = 0.14r_c$, and $\delta = 0.8$. Fig. 2 shows good agreement between the different meshes, especially grids 5, 6 and 7. Grid 5 was chosen to reduce the time and cost of simulations while providing sufficient accuracy. Moreover, the deformation of the studied grid and its adaptive refinement at $t = 1000$ are depicted in Fig. 4, demonstrating a smooth transient. The light blue and light orange show the solid and liquid regions, respectively, and the red line indicates the melting front.

5. Validation and verification

Previous studies were considered to examine the accuracy of the employed numerical modeling and validate the results of the present study. The experimental results of Kumar et al. [57] were

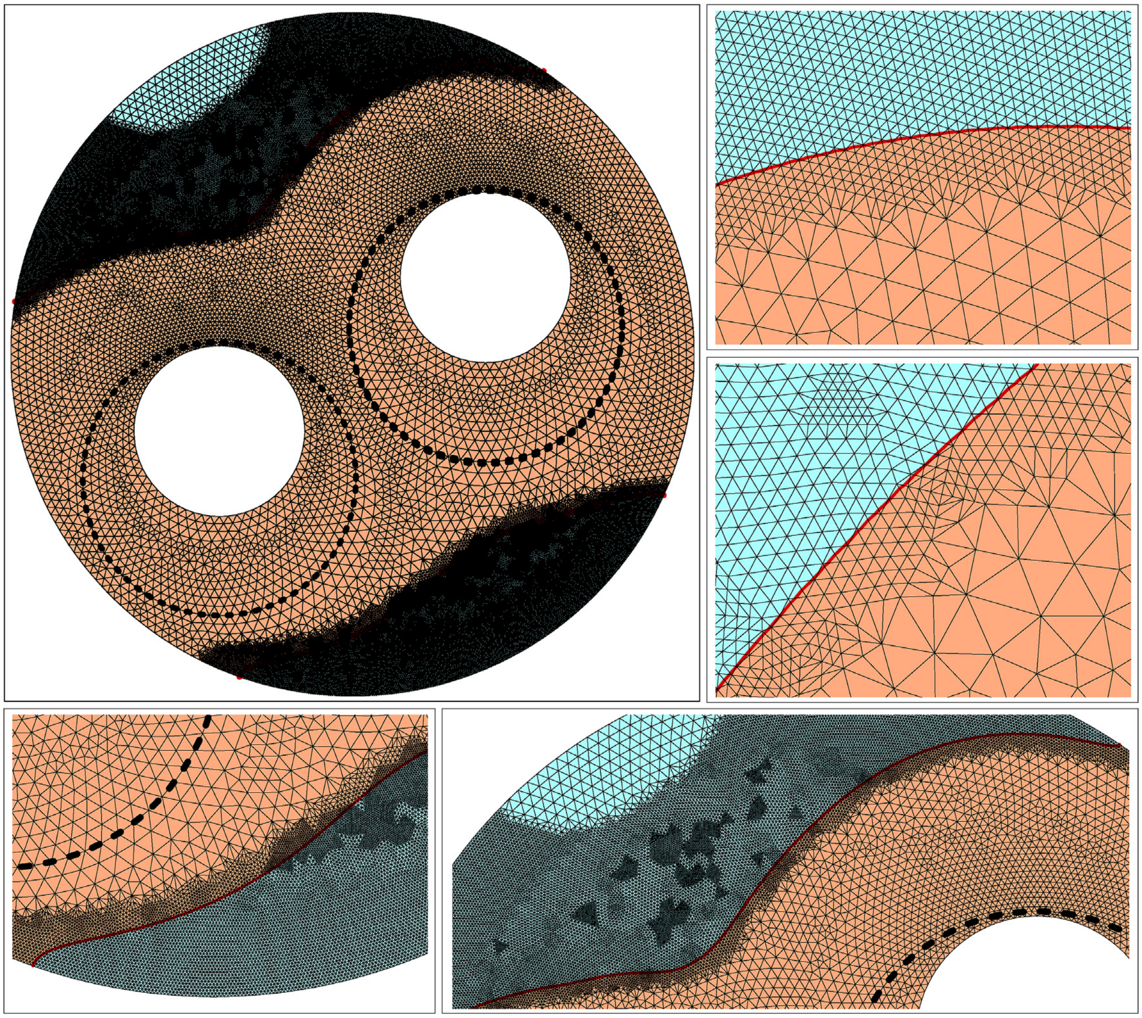

Fig. 4. The adopted gird for computations (Grid 5) at $t = 1000$s. The red line indicates the melting front, the light blue and light orange specify the solid and liquid regions, respectively. The dashed line represents the area of the porous medium. (For interpretation of the references to colour in this figure legend, the reader is referred to the Web version of this article.)

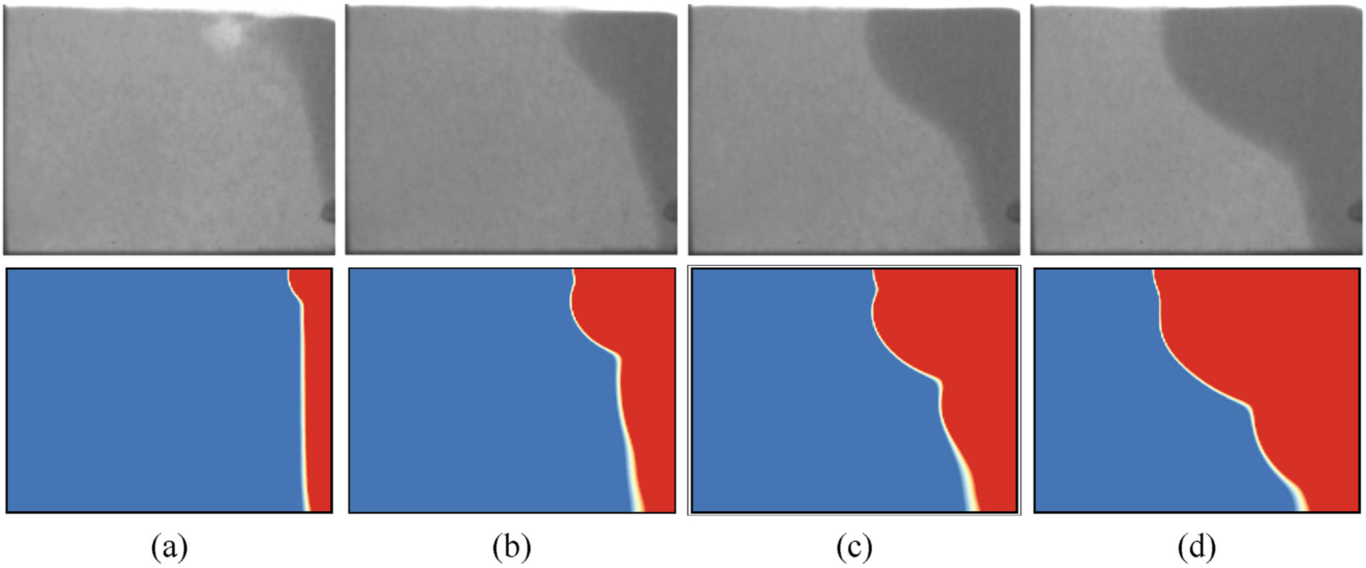

Fig. 5. the experimental results of Kumar et al. [57] (first row) and the numerical results of the current work (second row) for (a): $t = 139$s, (b): $t = 277$s, (c): $t = 416$s and (d): $t = 554$s.

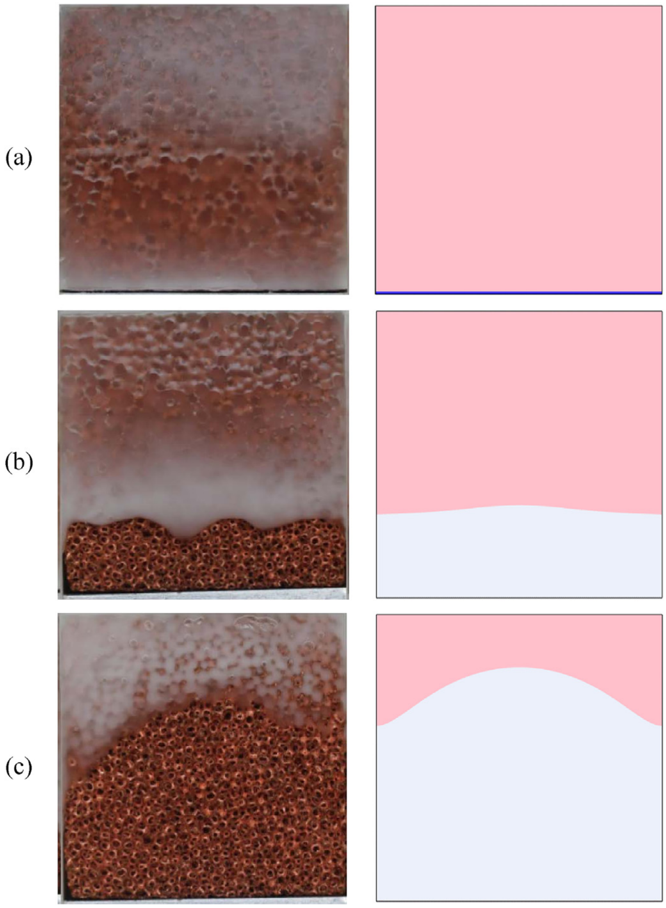

Fig. 6. The results presented in Ref. [50] (left) and the numerical outcomes of the current work (right) for (a): $t = 5400$ s (b): $t = 10800$ s and (c): $t = 16200$ s.

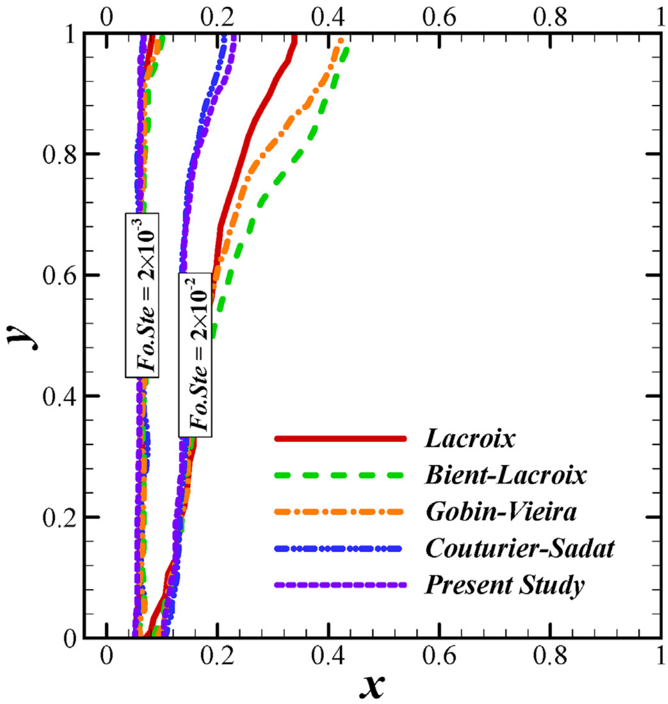

Fig. 7. A comparison between the results of the present study and literature review of [58].

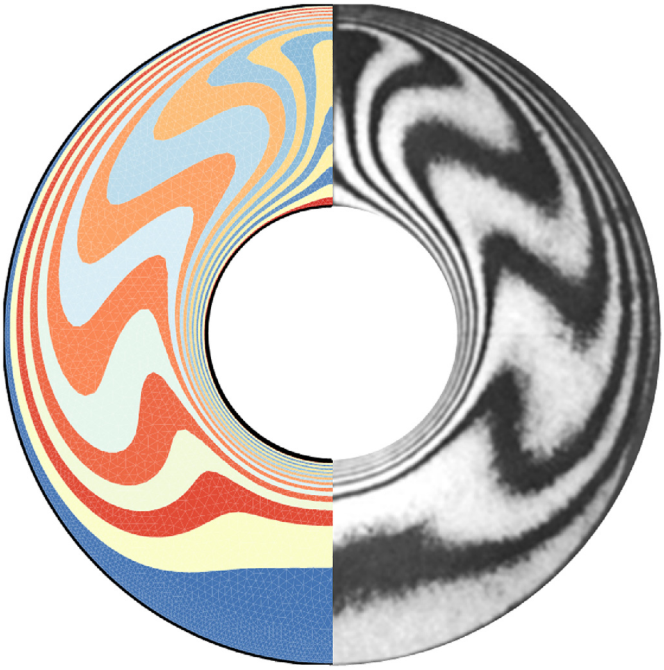

Fig. 8. Comparison between the isotherm of this study (left) and Ref. [64] (right).

considered as the first case for comparison. They investigated the solid-liquid interface in the melting process of lead, which was captured by neutron radiography of the flux. The vertical side-wall of their domain had a constant heat flux imposed, while the other walls were insulated. Fig. 5 demonstrates the melting front of the present work and the experimental results of Kumar et al. [57] at four different time instants with $Pr = 0.0236$, $Ste = 0.4$, $Ra = 1.4 \times 10^7$, and element heat flux of 16.3 kW/m^2. The results show qualitative agreement in the extent and the shape of the melting front. Second, the results of the current work are validated against the experimental study of Zheng et al. [50]. They examined melting heat transfer during the phase change of embedded paraffin wax in a metal foam. A cavity size of 0.1 m was filled with copper metal foam (pore size of 5 PPI), leading to a cavity porosity = 0.95. The left wall of the cavity was subjected to a heat flux $q = 1150$ W/m^2, while the other walls were insulated. The melting interface of the present work and the experimental results of Ref. [50] are shown in Fig. 6 at three time instants. Again the results show that the method captures the overall extent and large scale shape of the interface. Third, the melting front inside the cavity of the present study was compared with the graphs of Ref. [58]. Their extensive investigation was done into the melting of a base PCM (without any nanoparticle) within a square cavity in where the left and right vertical walls were considered at hot and cold temperatures ($T_h > T_c$), respectively, and two horizontal walls were insulated. The results were examined at $Ra = 1.25 \times 10^5$, $Pr = 50$ and two different values of dimensionless number $Fo.Ste$ ($Fo.Ste = 0.01$ and 0.002). The current findings in Fig. 7 are within the uncertainty present in the literature results. Finally, the experimental research of Kuehn and Goldstein [59] was considered to examine the natural convection heat transfer behavior. Their investigations were done to study the natural convection in the region between two horizontal cylinders. They considered water and air as the working fluid, and the ratio of annulus gap width (L) to the diameter of inner cylinder (D_i) was $L/D_i = 0.8$. The comparison of the isotherm contours of the current work and the experimental results of Ref. [59] are depicted in Fig. 8, when $Pr = 0.706$ and $Ra = 4.7 \times 10^4$

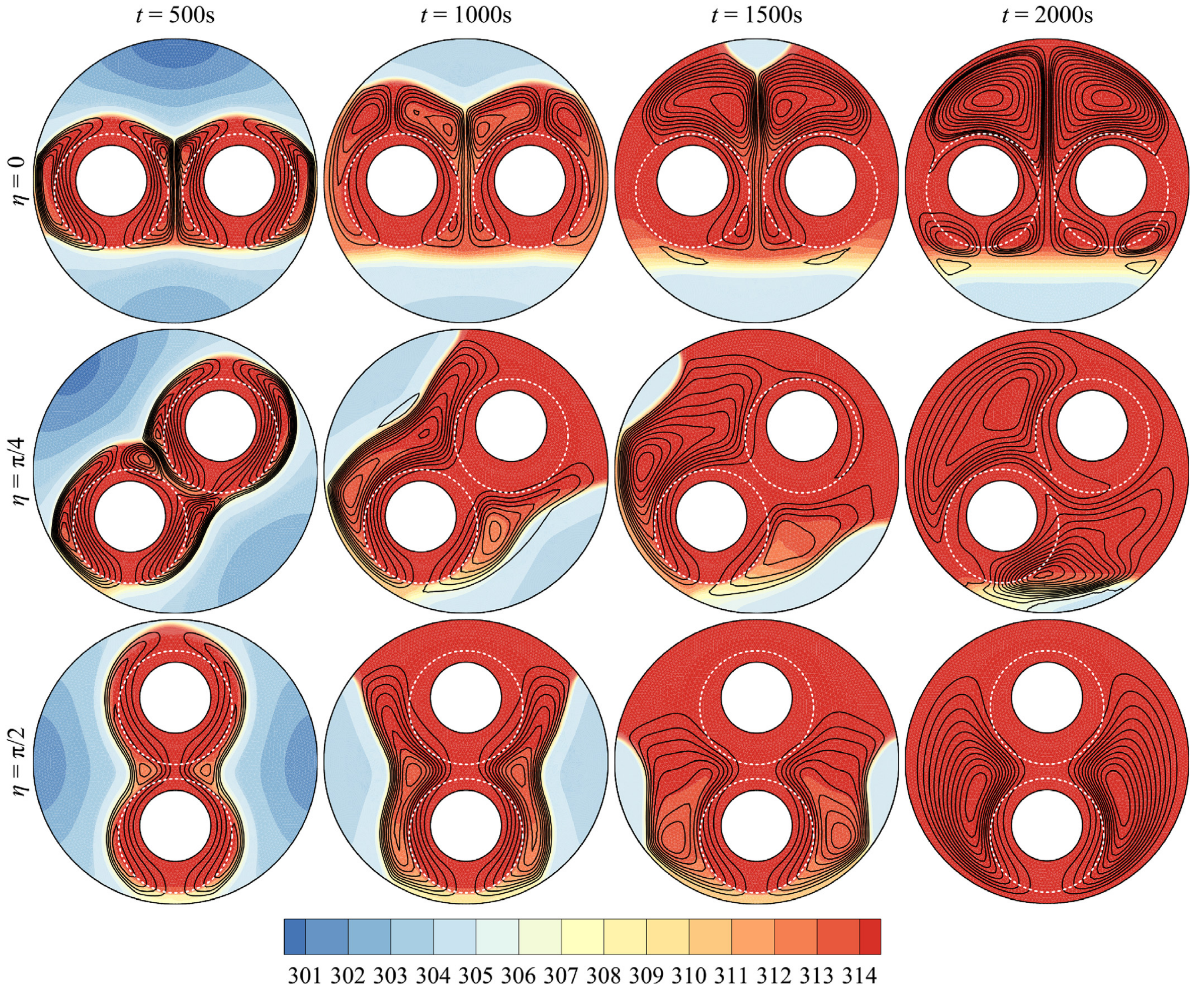

Fig. 9. Influence of the angle η on the isotherms and streamlines at different charging time ($\omega_{GO} = 0.04$, $\omega_{Cu} = 0.0$, $e = 0.07r_c$, $\delta = 0.8$): (a) $t = 500$ s, (b) $t = 1000$ s, (c) $t = 1500$ s and (d) $t = 2000$ s.

demonstrating a good agreement.

6. Results and discussion

The outcomes of the present study are divided into three parts. First, the influence of each parameter on the patterns of melting (i.e., contours of isotherms and streamlines) and also the melt volume fraction are assessed and discussed individually (while keeping all other parameters unchanged). The second part is devoted to the effect of each parameter on the thermal capacity and charging power of the LHTES system. The last part discusses the trade-off between the thermal capacity of the LHTES system and its charging power. The parameters studied in this work are the eccentricity of partial metal foam ($0 \leq e \leq 0.14\, r_s$), its porosity ($0.8 \leq \varepsilon \leq 1$), angle of the heat pipes with the horizon ($0.0 \leq \eta \leq 90°$) and the volume fraction of the nano-additives ($0 \leq \omega_{na} \leq 0.08$).

6.1. Charging patterns

Fig. 9 depicts the impact of heat pipe angle on the isothermal lines and streamlines at different charging times of 500s, 1000s, 1500s, and 2000s. The melting process initiates around the surface of the heat pipes, and as time elapsed, the phase change proceeds, and the melt volume fraction increases. Buoyancy is the driving force for the natural convection flow of the melted PCM in the storage. The liquid PCM around the hot surfaces expands and rises. In consequence, the flow of the liquid around the hot surfaces is always upward. With increasing melted volume fraction (*MVF*), natural convection intensifies and the strength of vortices increases. It can be seen that the geometry of the storage remarkably influences the pattern of streamlines and hence, the way that the LHTES charges. When $\eta = 0$, four separate vortices can be found around the hot surfaces at the early stages of the melting process ($t < 1000$s). Owing to the symmetry of the storage for the case of $\eta = 0$, the strength and pattern of streamlines of the left and right half of the storage are exactly the same. It is evident that for $\eta = 0$ and $\pi/4$, the strength of the formed vortices on the upper portion of the storage are much higher than those in the lower part. Hence, the melting rate in the upper portions is considerably higher than the lower parts. By increasing the angle η, the mean distance

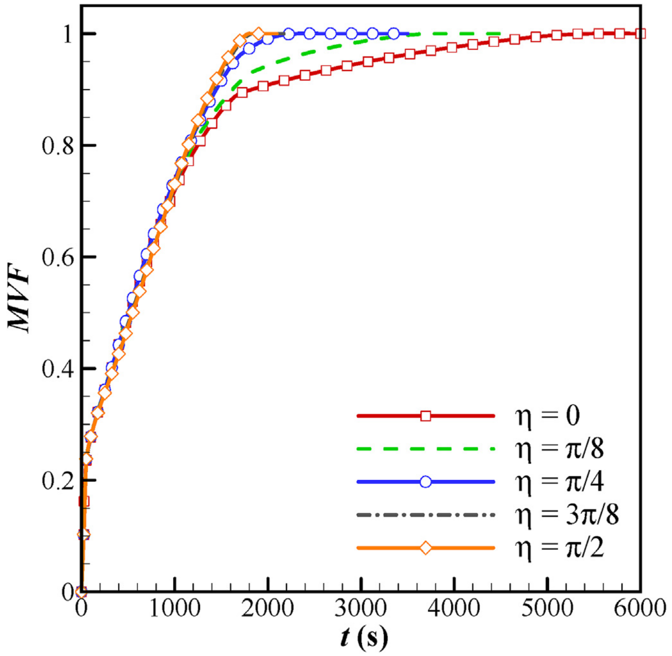

Fig. 10. Variaiton of the liquid fraction during charging process for different values of angel η ($\omega_{GO} = 0.04$, $\omega_{Cu} = 0.0$, $e = 0.07r_c$, $\delta = 0.8$).

between the hot surfaces and the bottom part of the storage decreases. This accelerates the melting process, and thus the full charging time of the storage is below 2000s when $\eta = \pi/2$.

Fig. 10 outlines the melted volume fraction of the PCM for different values of angle η. As seen, owing to the presence of the partial metal foam around the hot surfaces, the melting rate is quite high at the beginning of the charging process ($t < 100-150$s). The impact of angle η is more pronounced when the melted volume fraction (*MVF*) approaches around 0.8, and the natural convection in the storage becomes stronger.

Figs. 11 and 12 outline the influence of porosity and eccentricity of the porous medium on the isothermal lines and streamlines at four different melting times. Increasing the porosity of the porous medium has a double-sided impact on the melting rate. On the one hand, it reduces the effective thermal conductivity of the storage and thus retards the conduction mode of heat transfer. On the other hand, higher porosity causes higher liquid flow in the storage and therefore a higher rate of convection heat transfer. As expected, increasing porosity of the utilized porous medium strongly decreases the melting rate (Fig. 11).

The eccentricity of the porous medium also plays a significant role in the melting rate of the phase change material (Fig. 12), in that increasing the eccentricity of the porous medium increases the effective thermal conductivity of the storage, and hence the conduction mechanism intensifies in the lower portion of the cavity. Since the melting process is governed by convection on the upper parts of the storage, increasing eccentricity is seen to accelerate the overall charging process.

Fig. 13 (a) and (b) illustrate the variation of melted volume fraction of the NePCM with porosity and eccentricity of the porous medium, respectively. It can be seen that the slope of *MVF* variation with time for the case of $\delta = 1.0$ is much lower than the other cases. This illustrates that the presence of the porous metal foam can considerably intensify the rate of melting. When all of the PCM in the porous zone melts, the phase change process continues normally. Nonetheless, compared to the case of without metal foam ($\delta = 1.0$), the melting rate proceeds more rapidly, indicating that the presence of a partial metal foam impacts the whole of the phase change process. In fact, owing to the presence of the utilized partial metal foam, the thermal resistance is reduced, and hence the rate of heat transfer intensifies throughout the enclosure. Fig. 13 (b) shows that increasing the eccentricity of the porous medium only affects the final stages of the phase transition (*MVF* > 0.85). The melting rate (the slope of *MVF* with time) increases as the eccentricity of the porous medium increases. In fact, the phase change process slows in the bottom portion of the enclosure. As a result of the exerted buoyancy force, liquid PCM with a high temperature rises, and only melted PCM with relatively lower temperature can be found around the melting interface at the bottom of the storage. Liquid PCM with lower temperature retards the phase transition in this region. Increasing the eccentricity of the porous medium enhances the conduction mechanism of the heat transfer in the bottom parts and thus amplifies the melting rate.

Figs. 14 and 15 show the impact of the volume fraction of two different nano-additives (Cu and GO) on the patterns of melting. For the Cu nano-particles, the volumetric heat capacity, and for the GO nano-particles, the thermal conductivity is very high. As a result, adding Cu nano-additive to the base PCM enhances the advection mechanism in the melting process. On the other hand, the conduction mode of heat transfer is boosted for NePCM comprising GO nano-particles. For the studied set of parameters, the presence of either Cu or GO nano-additive is shown in Figs. 14 and 15 to increase the phase transition. Moreover, no visible difference can be found between the isothermal and streamlines of NePCM containing Cu and GO nano-additives.

Fig. 16 (a) and (b) present the dependency of the melt fraction on the type of nano-additive. It is evident that the rate of phase change for the case of NePCM is moderately higher than the case of pure PCM. However for each volume fraction, the melting time of both CU and GO nano-particles are approximately the same.

6.2. Capacity and average charging power of the LHTES

In this section the impact of the surveyed parameters on the capacity and average charging power of the LHTES is analyzed. It should be noted that the capacity of the storage is the sum of both latent and sensible forms of energy that could be stored in the storage before the melting process is complete. In other words, the capacity of the LHTES is the total energy stored in a full charging cycle. Correspondingly, the average charging power is the total capacity of the storage divided by full melting time. The average charging power, in fact, indicates how fast the storage is being charged.

Fig. 17 shows the impact of angle η on the capacity and charging power of the thermal storage. Rotating the hot surfaces of heat pipes in the enclosure does not alter the volume of the PCM (or NePCM), and thus the latent capacity of the storage remains unchanged. However, the sensible component of the total capacity slightly increases when η increases from 0 to $\pi/2$, as the average temperature of the phase change material increases. The average charging power of the LHTES increases markedly and the melting time decreases considerably when the heat pipes are positioned vertically. As discussed previously, this is due to the fact that with increasing angle η, the average distance between the hot surfaces and the lower portion of the enclosure decreases. In consequence the phase change takes place faster, and charging power intensifies. Fig. 17 indicates that the geometry of the LHTES can play an important role in its charging time and hence, charging power.

Fig. 18 outlines the influence of the porosity of the porous medium on the capacity and the average charging power of the storage. By increasing the porosity of the porous medium, the volume of the phase change material inside the enclosure is raised and the

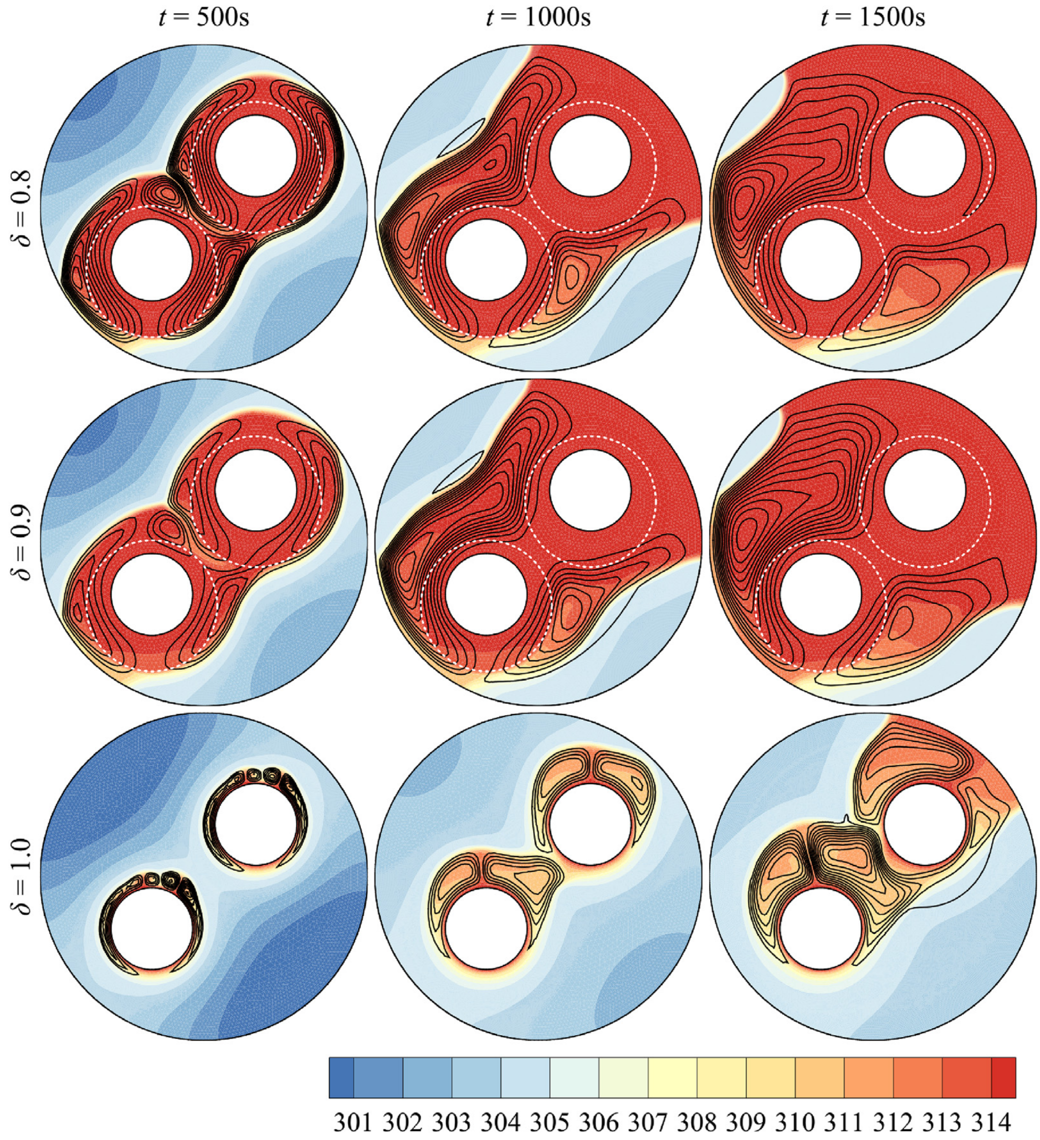

Fig. 11. Influence of the porosity of porous medium on the isotherms and streamlines at different charging time ($\eta = \pi/4$, $\omega_{GO} = 0.04$, $\omega_{Cu} = 0.0$, $e = 0.07r_c$): (a) $t = 500$ s, (b) $t = 1000$ s, (c) $t = 1500$ s and (d) $t = 2000$ s.

latent heat capacity of the storage is amplified, while the sensible capacity of the storage shrinks. This is plausible in that the volume of the porous medium decreases as δ increases. Since the thermal conductivity of the porous medium is much higher than the PCM, the porous medium can be considered isothermal with an approximate temperature of $T = T_h$. In consequence, reducing the amount of porous medium leads to a slight reduction in the sensible portion of thermal capacity. This can be explained by the fact that by increasing the porosity of the porous medium, the mass of the PCM increases, and hence, a higher portion of the total absorbed energy would be stored as latent heat. As a result, the share of sensible heat energy decreases.

The average charging power shows a non-monotonic behavior with increasing porosity. As seen in Fig. 18 as δ increases, the average charging power first increases and then decreases. This can be explained by considering both the thermal capacity and melting time of the storage. With increasing porosity, the capacity of the storage is increased, but the corresponding melting time rises since the effective thermal conductivity of the cavity declines. Consequently, by increasing the porosity of the porous medium from 0.8 to 0.9, the charging power of the storage is enhanced. This means that the increment rate of the capacity is higher than that of the melting time. However with further increase in the porosity, the melting time surges, and thus, the charging power drops considerably. According to Fig. 18, within the range of studied parameters, the highest charging power can be obtained when $\delta = 0.9$.

Fig. 19 illustrates how the eccentricity of the porous medium affects the thermal capacity and also the charging power of the LHTES. The volume of PCM remains constant with increasing eccentricity of the porous matrix, and hence, the latent heat of the storage remains static. A very slight increase in the sensible component of the thermal capacity can be found when e increases. Nonetheless, the charging power of the LHTES is significantly enhanced when the eccentricity rises. For the set of studied parameters and the geometry, the results show that the charging power can be augmented to around 60% when the eccentricity of the porous matrix increases. This, as explained above, is attributed to the mean distance between the hot surfaces and the lower parts of the enclosure. Fig. 19 reveals that the locality of the solid matrix around the hot surface can improve the charging power of an

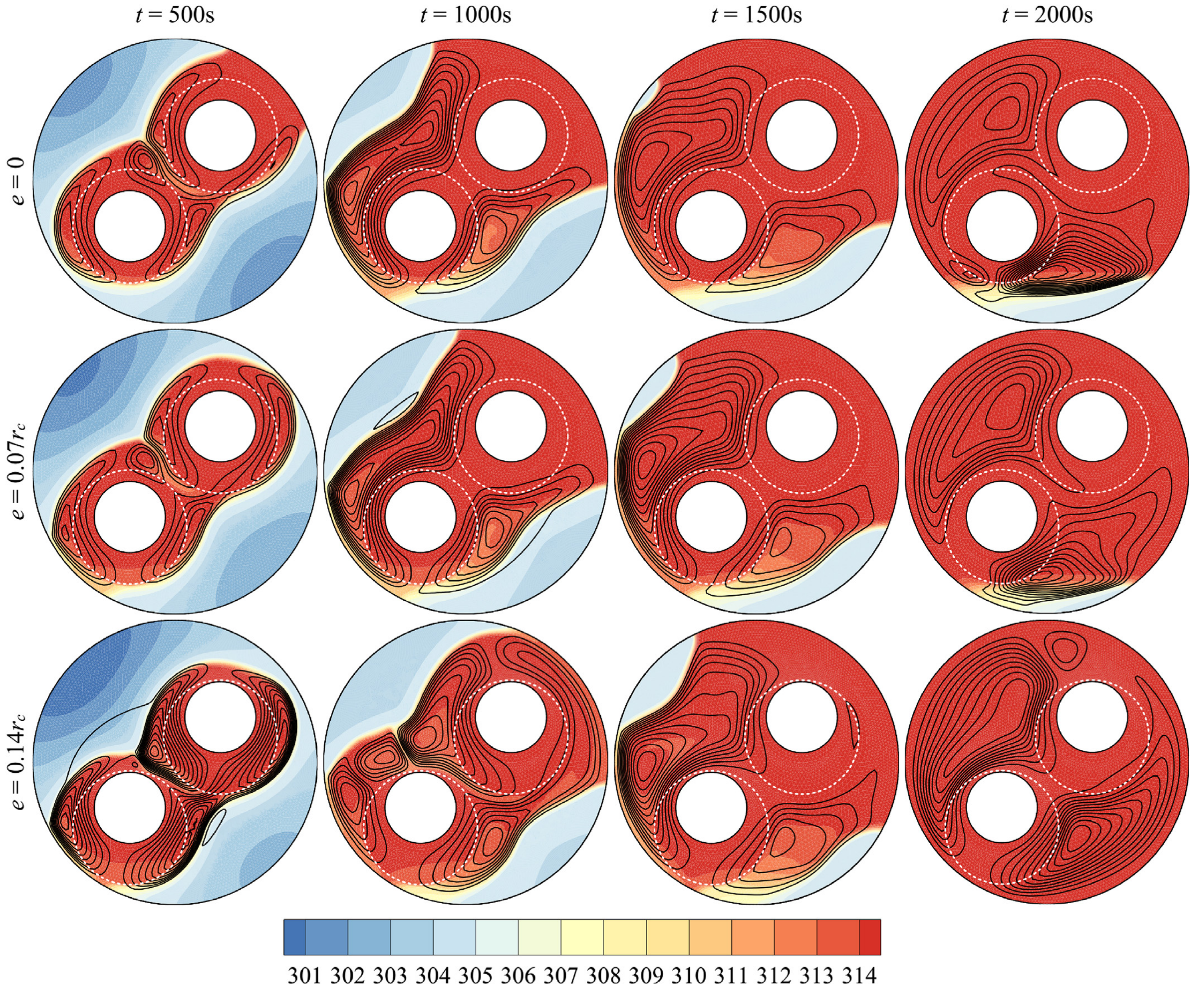

Fig. 12. Influence of the eccentricity of the porous medium on the isotherms and streamlines at different charging time ($\eta = \pi/4$, $\omega_{GO} = 0.04$, $\omega_{Cu} = 0.0$, $\delta = 0.9$): (a) $t = 500$ s, (b) $t = 1000$ s, (c) $t = 1500$ s and (d) $t = 2000$ s.

LHTES to a great extent.

Fig. 20 outlines the variation of the thermal capacity and charging power of the thermal storage with the volume fraction of the studied nano-additives, i.e., Cu and GO. Similar trends can be observed for both of the overall thermal capacity and the charging power of the Cu- and GO-PCM when the volume fraction of the nanoparticles increases. Adding nano-particles to the pure PCM reduces the volume fraction of the PCM and hence reduces the overall latent heat capacity of the storage. Moreover the effective thermal conductivity of the storage increases due to the higher thermal conductivity of the nano-additives. As a result, the melting process proceeds faster and the charging power of the LHTES increases. It can be seen that for Cu nano-additives, the sensible heat capacity of the TES increases, while its counterpart for GO nanoparticles exhibits a decreasing trend. In fact, the mass of PCM decreases as the nano-additives volume fraction increases. As a result, a higher share of heat is stored in the form of sensible heat (higher average temperature). The volumetric heat capacity (ρC_p) of the Cu and GO nano-additives are lower than the capric acid (PCM). With increasing volume fraction of both nano-additives, the average volumetric heat capacity of the storage decreases. According to Table 1, the value of ρC_p for GO nano-particles is much lower than the Cu. In other words, for GO nano-additives, the rise in the average temperature cannot compensate for the reduction of the volumetric heat capacity of the storage. Consequently, according to Eq. (22), the sensible heat capacity of the storage reduces when GO nano-particles are incorporated.

6.3. Comparison with constant volume of PCM

In the previous sections, the impact of the key parameters on the melting pattern and the thermal performance of the LHTES was assessed. It was shown that the presence of both partial metal foam and also nano-particles of Cu and GO can enhance the charging power and reduce the thermal capacity of the storage. In fact, it was found that there is an inverse relationship between the capacity of the storage and the corresponding charge time (or charging power). However the results obtained from the variation of each parameter

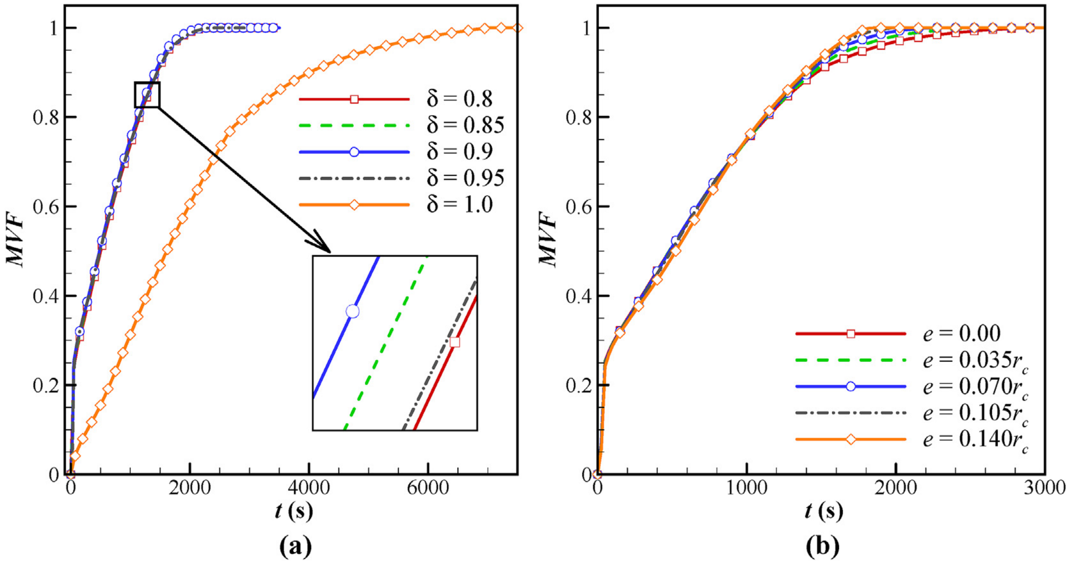

Fig. 13. Variaiton of the liquid fraction during charging process ($\eta = \pi/4$, $\omega_{GO} = 0.04$, $\omega_{Cu} = 0.0$): (a) porosity ($e = 0.07r_c$) and (b) eccentricity ($\delta = 0.9$) of porous medium.

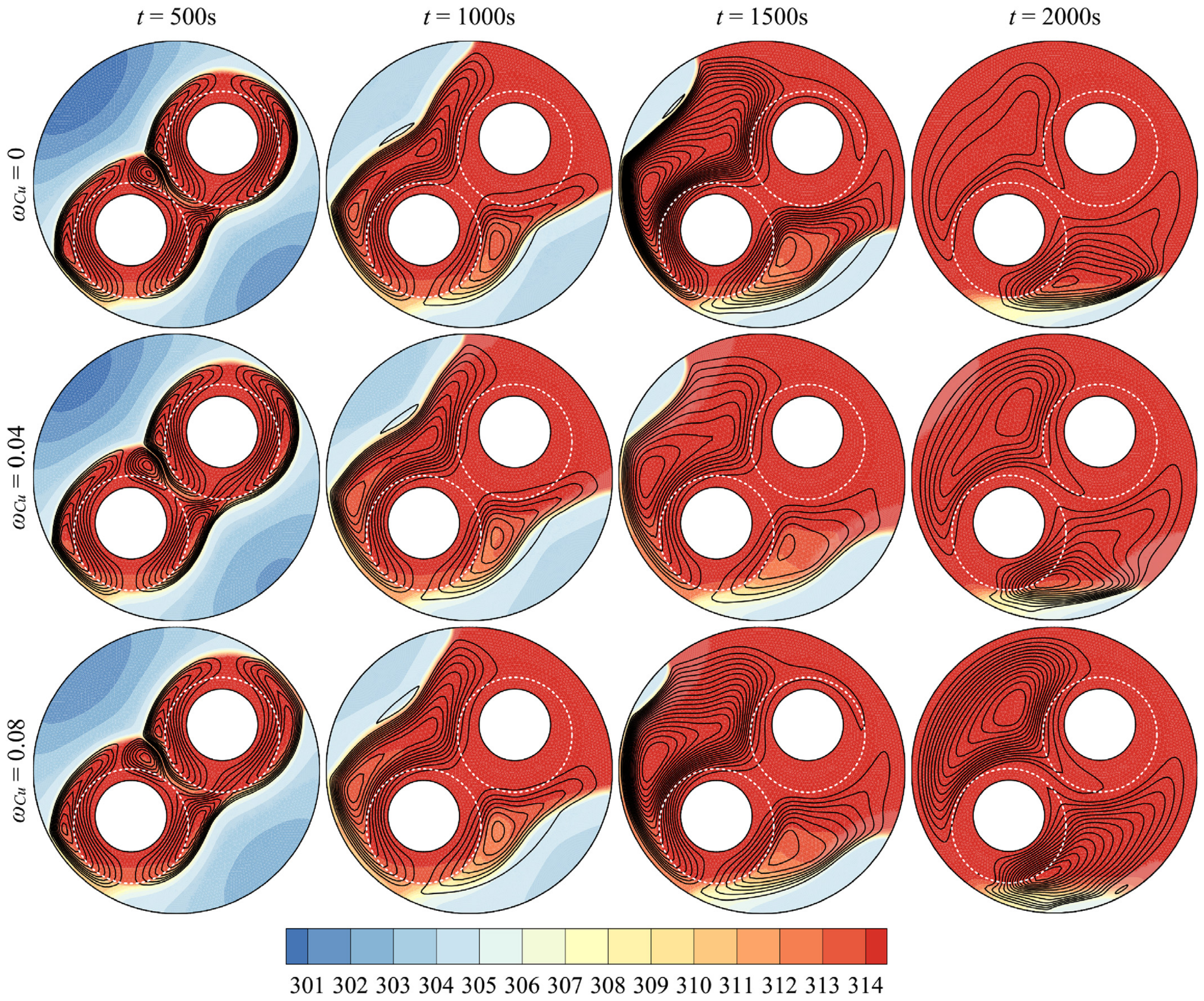

Fig. 14. Influence of the volume fraction of Cu nano-additive on the isotherms and streamlines at different charging time ($\eta = \pi/4$, $\delta = 0.9$, $\omega_{GO} = 0.0$, $e = 0.07r_c$): (a) $t = 500$ s, (b) $t = 1000$ s, (c) $t = 1500$ s and (d) $t = 2000$ s.

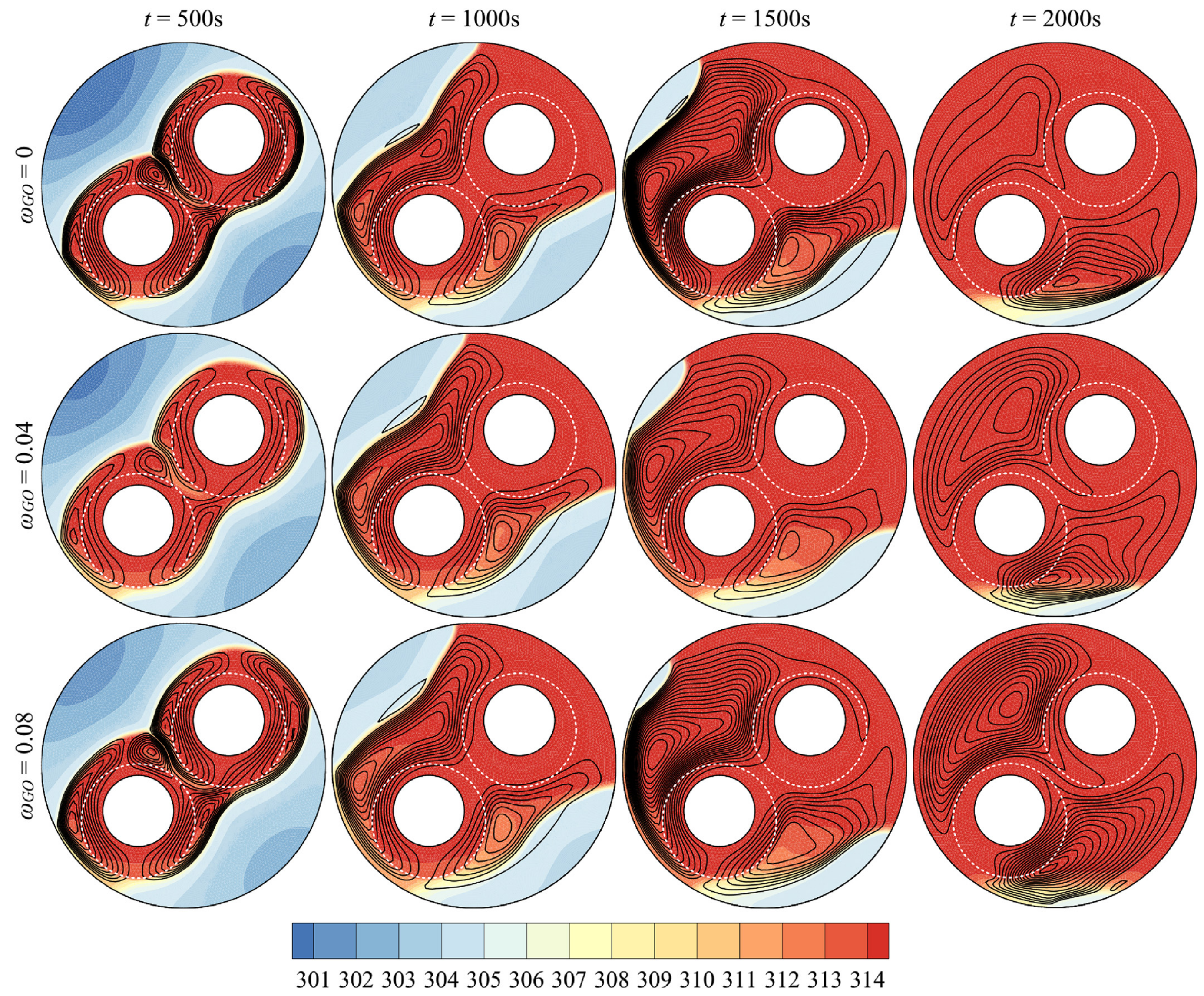

Fig. 15. Influence of the volume fraction of GO nano-additive on the isotherms and streamlines at different charging time ($\eta = \pi/4$, $\delta = 0.9$, $\omega_{Cu} = 0.0$, $e = 0.07r_c$): (a) $t = 500$ s, (b) $t = 1000$ s, (c) $t = 1500$ s and (d) $t = 2000$ s.

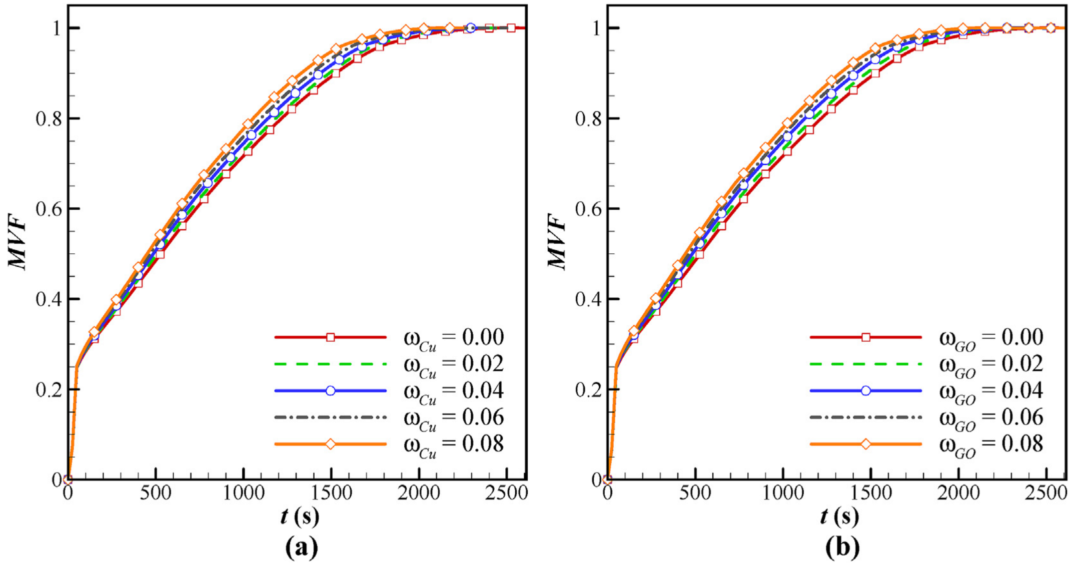

Fig. 16. Variaiton of the liquid fraction during charging process ($\eta = \pi/4$, $\delta = 0.9$, $e = 0.07r_c$) with: (a) Cu nano-additive ($\omega_{GO} = 0.0$) and (b) GO nano-additive ($\omega_{Cu} = 0.0$).

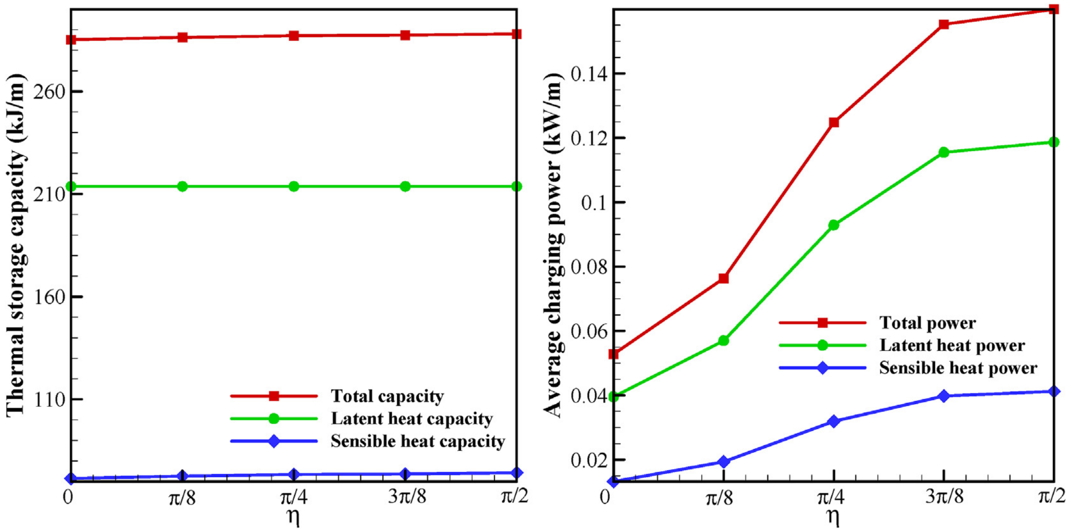

Fig. 17. Dependency of the average thermal storage capacity (left) and average charging power charging process (right) on the angle η ($\omega_{GO} = 0.04$, $\omega_{Cu} = 0.0$, $e = 0.07r_c$, $\delta = 0.8$).

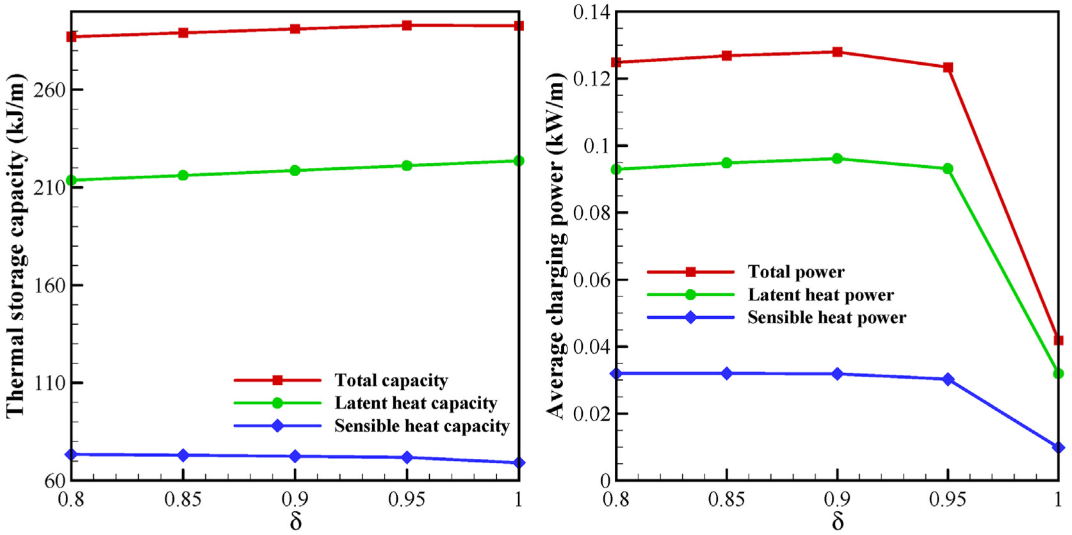

Fig. 18. Dependency of the average thermal storage capacity (left) and average charging power charging process (right) on the porosity of the porous medium ($\eta = \pi/4$, $\omega_{GO} = 0.04$, $\omega_{Cu} = 0.0$, $e = 0.07r_c$).

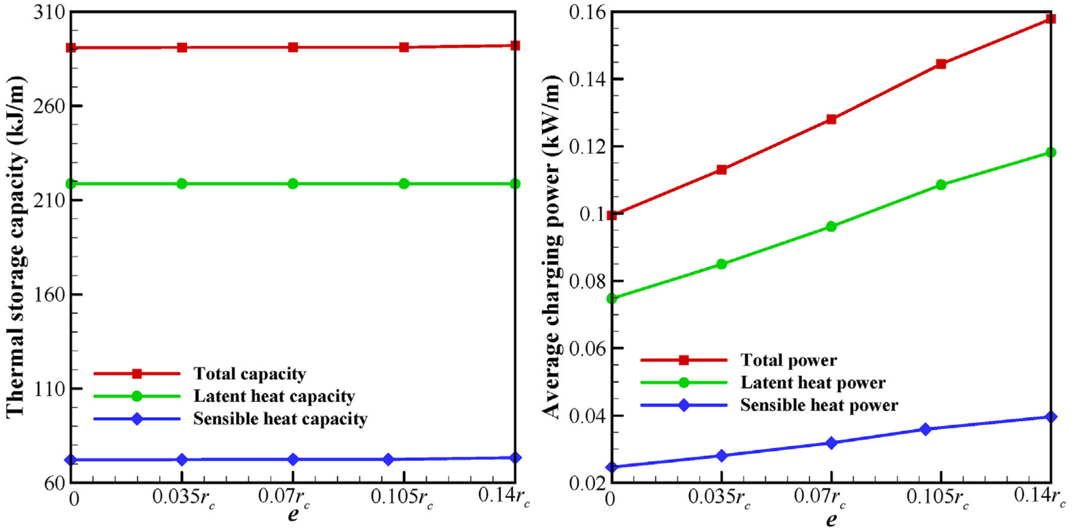

Fig. 19. Dependency of the average thermal storage capacity (left) and average charging power charging process (right) on the eccetricity of porous medium ($\eta = \pi/4$, $\omega_{GO} = 0.04$, $\omega_{Cu} = 0.0$, $\delta = 0.9$).

cannot be directly compared as the mass of the PCM varied from case to case. To get a better estimation of how each parameter affects the thermal capacity and melting time of the storage, a comparison has been carried out in which the mass (volume) of the phase change material is constant. Details of the utilized parameters are presented in Table 3. The radii of the partial metal foams were considered to be constant ($r_p/r_s = 0.4$). As a result, the volume fraction of the phase change material was obtained as 95.4%. With this value fixed, five different cases with different combinations of partial metal foam and nano-additives, namely cases 2 to 6, are taken into account for comparison. Two more cases are assessed. In case 1, as a reference case, the storage is fully saturated with pure PCM. Moreover, the storage is completely filled with metal foam for case 7.

Fig. 21 compares the thermal capacity of the storage for the seven surveyed cases. For simplicity, the outcomes are normalized with respect to the case 1 (pure PCM). As mentioned above, the mass of the PCM for all cases of 2–7 is the same, and there are only differences between sensible heat capacity of the storage. The capacity of the storage was found to retard significantly (around 17%) when fully filled with a porous medium with a porosity of 0.8. Employing partial metal foam with a volume fraction of 4.6% (without nano-additives) decreases the thermal capacity of the storage to about 2%. Moreover, the results show that the combination of partial metal foam and nano-additives of Cu and GO (cases 3, 4, and 6) are approximately similar in terms of the total capacity of the LHTES. Using nano-additives of Cu only results in the lowest capacity of the storage.

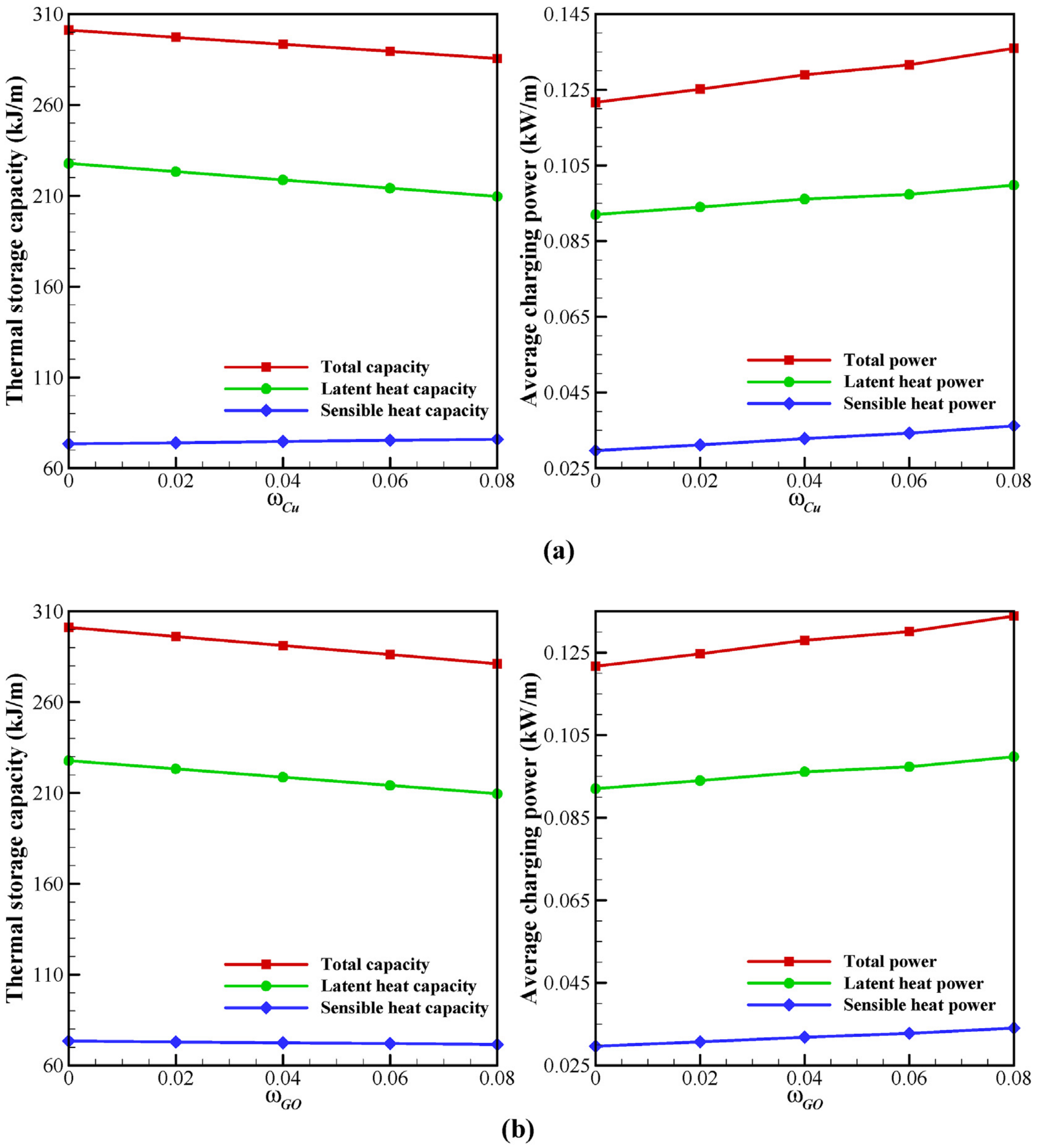

Fig. 20. Dependency of the average thermal storage capacity (left) and average charging power charging process (right) on the volume fraction of (a) Cu ($\omega_{GO} = 0.0$) and (b) GO ($\omega_{Cu} = 0.0$) nano-additives ($\eta = \pi/4$, $\delta = 0.9$, $e = 0.07r_c$).

Table 3
Specifications of the studied cases ($\eta = \pi/4$, $e = 0.14r_c$).

Case No.	ω_{PCM}	ω_{pm}	ω_{Cu}	ω_{GO}	r_p/r_s	δ	Description
1	100%	0%	0%	0%	0.0	1.0	Pure PCM
2	95.4%	4.6%	0%	0%	0.4	0.8	Partial metal foam without nano-additives
3	95.4%	2.3%	2.3%	0%	0.4	0.9	Partial metal foam with Cu nano-additive
4	95.4%	2.3%	0%	2.3%	0.4	0.9	Partial metal foam with GO nano-additive
5	95.4%	0%	4.6%	0%	0.4	0.9	Cu composite PCM without metal foam
6	95.4%	0%	0%	4.6%	0.4	0.9	GO composite PCM without metal foam
7	80%	20.0%	0%	0%	1.0	0.8	Full metal foam

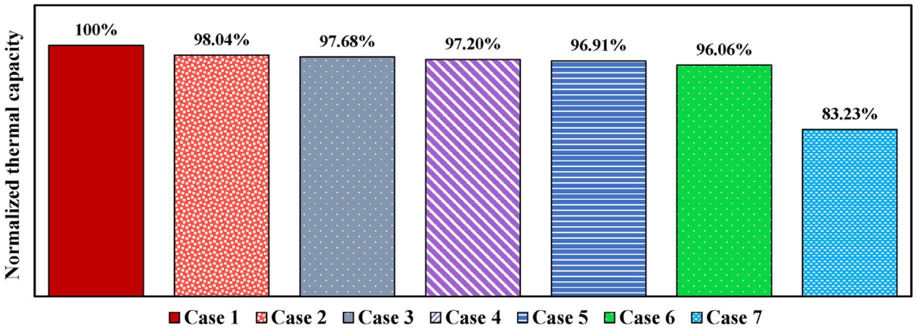

Fig. 21. Comparison between the normalized thermal capacity of the seven studied cases detailed in Table 3.

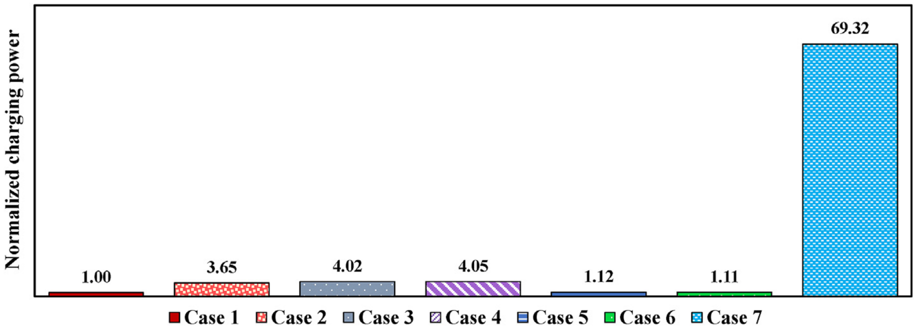

Fig. 22. Comparison between the normalized charging power of the seven studied cases detailed in Table 3.

Fig. 22 presents the normalized charging power with respect to the case of pure PCM (case 1). As expected, the highest charging power corresponds to the case of full copper foam-PCM composite (case 7) with power around 70 times higher than the case of full PCM (case 1). As discussed, this performance augmentation is achieved at the cost of around 17% reduction in the thermal capacity of the storage. Interestingly, with a constant volume fraction of the PCM, the charging rates varies considerably for cases 2 to 7. The case of partial metal foam without nano-additives (case 2) has a charging power 3.65 times that of the case without copper foam (case 1), at the expense of only 2% reduction in the thermal capacity of the LHTES. In addition, compared to case 2, adding nano-sized particles of Cu and GO has a lower efficiency since with approximately equal capacity of the storage, their charging power is much lower than for case 2. On the other hand, hybrid utilization of the enhancement methods, i.e., metal foam and nano-additives, provides better performance than each case separately. Finally, it is shown that the GO nano-particles have slightly better performance than Cu nano-additives when employed in a hybrid enhancement approach.

7. Conclusion

The charging process of a phase change substance, namely capric acid, in a circular thermal energy storage with a two-pass heat pipe has been numerically studied. The enthalpy-porosity method has been employed to model phase transition. In addition, an adaptive mesh refinement technique has been used to precisely track the melting front with time. The efficiency of hybrid heat transfer enhancement of a latent heat thermal energy storage via a combination of partial copper foam and Cu/GO nano-additives has been analyzed. The effects of the angle of the heat pipes with the horizon, porosity, and eccentricity of the metal foam and volume fraction of the Cu/GO nano-additives have been investigated and discussed in detail. The principal outcomes of the study can be summarized as follows:

1. The position of the heat pipes (angle η) significantly affects the average charging power of the thermal storage. This is because the average distance between the hot surfaces and the lower portion of the enclosure decreases with increasing angle η.

2. By increasing the porosity of the copper foam, the volume (mass) of the PCM within the storage rises, resulting in enhancement of its latent heat capacity. On the other hand, the average charging power is a non-monotonic function of the porosity. By increasing δ, the average charging power first increases ($\delta < 0.9$) and then decreases ($\delta > 0.9$). Moreover, for the set of studied parameters, the highest charging power can be obtained when $\delta = 0.9$.
3. The volume of PCM remains constant with increasing eccentricity of the porous matrix. As a result, the eccentricity of the partial metal foam has a negligible impact on the thermal capacity of the storage. However, the average charging power of the LHTES can be enhanced to around 60% with the appropriate eccentricity.
4. Adding nano-particles to the pure PCM reduces the volume fraction of the PCM, and thus decreases the overall latent heat capacity of the storage. On the other hand, the effective thermal conductivity of the storage increases, which leads to an increment in the charging power of the LHTES.
5. The capacity of the storage retards significantly (around 17%) when fully filled with a porous medium with a porosity of 0.8. Moreover, using a sole partial metal foam with a volume fraction of 4.6% is shown to decrease the thermal capacity of the storage by about 2%.
6. The highest charging power can be obtained in the case of full copper foam-PCM composite (case 7) with power around 70 times higher than the case of full PCM (case 1). This performance augmentation was achieved at the cost of approximately 17% reduction in the thermal capacity of the storage.
7. For a constant volume fraction of PCM, the charging rate varies considerably when a single or combination of enhancement methods are employed. The case of partial metal foam without nano-additives (case 2) was shown to have a charging power of 3.65 time higher than the case without copper foam (case 1), at the expense of only 2% thermal capacity of the LHTES.
8. For a given volume fraction of the PCM, the sole employment of the nano-sized particles of Cu and GO has a lower efficiency than utilizing partial metal foam.
9. Hybrid application of the thermal enhancement methods, i.e., metal foam and nano-additives, is more efficient than each approach individually. In addition, incorporation of the GO nano-particles has slightly better performance than Cu nano-additives in a hybrid enhancement approach.

Statement

S.M. Hashem Zadeh: Conceptualization, Methodology, Writing-Original draft preparation, Writing - Review & Editing, Investigation, Validation. S.A.M. Mehryan: Methodology, Writing- Original draft preparation, Writing - Review & Editing. M. Ghalambaz: Supervision, Conceptualization, Methodology, Writing - Review & Editing, Investigation, Validation. M. Ghodrat: Methodology, Writing- Original draft preparation, Writing - Review & Editing. J. Young: Methodology, Writing- Original draft preparation, Writing - Review & Editing. A. Chamkha: Conceptualization, Writing - Review & Editing.

Declaration of competing interest

The authors declare that they have no known competing financial interests or personal relationships that could have appeared to influence the work reported in this paper.

References

[1] Tao YB, He Y-L. A review of phase change material and performance enhancement method for latent heat storage system. Renew Sustain Energy Rev 2018;93:245–59.
[2] Michels H, Pitz-Paal R. Cascaded latent heat storage for parabolic trough solar power plants. Sol Energy 2007;81(6):829–37.
[3] Fang M, Chen G. Effects of different multiple PCMs on the performance of a latent thermal energy storage system. Appl Therm Eng 2007;27(5):994–1000.
[4] Dhaidan NS, Khodadadi JM. Improved performance of latent heat energy storage systems utilizing high thermal conductivity fins: a review. J Renew Sustain Energy 2017;9(3):034103.
[5] Wang T-H, Yang T-F, Kao C-H, Yan W-M, Ghalambaz M. Paraffin core-polymer shell micro-encapsulated phase change materials and expanded graphite particles as an enhanced energy storage medium in heat exchangers. Adv Powder Technol 2020 June;31(6):2421–9. https://www.sciencedirect.com/science/article/abs/pii/S092188312030128X.
[6] Li W, Zhang D, Jing T, Gao M, Liu P, He G, et al. Nano-encapsulated phase change material slurry (Nano-PCMS) saturated in metal foam: a new stable and efficient strategy for passive thermal management. Energy 2018;165:743–51.
[7] Li W, Wan H, Lou H, Fu Y, Qin F, He G. Enhanced thermal management with microencapsulated phase change material particles infiltrated in cellular metal foam. Energy 2017;127:671–9.
[8] Hashem Zadeh Seyed M, Mehryan SAM, Islam MS, Ghalambaz M. Irreversibility analysis of thermally driven flow of a water-based suspension with dispersed nano-sized capsules of phase change material. Int J Heat Mass Tran 2020;155:119796.
[9] Alehosseini E, Jafari SM. Micro/nano-encapsulated phase change materials (PCMs) as emerging materials for the food industry. Trends Food Sci Technol 2019;91:116–28.
[10] Chandel SS, Agarwal T. Review of current state of research on energy storage, toxicity, health hazards and commercialization of phase changing materials. Renew Sustain Energy Rev 2017;67:581–96.
[11] Qiu L, Zhu N, Feng Y, Michaelides EE, Żyła G, Jing D, et al. A review of recent advances in thermophysical properties at the nanoscale: from solid state to colloids. Phys Rep 2020;843:1–81.
[12] Mahian O, Kolsi L, Amani M, Estellé P, Ahmadi G, Kleinstreuer C, et al. Recent advances in modeling and simulation of nanofluid flows-Part I: fundamentals and theory. Phys Rep 2019;790:1–48.
[13] Mahian O, Kolsi L, Amani M, Estellé P, Ahmadi G, Kleinstreuer C, et al. Recent advances in modeling and simulation of nanofluid flows—Part II: Applications. Phys Rep 13 February 2019;791:1–59. https://www.sciencedirect.com/science/article/abs/pii/S0370157318303296.
[14] Wang J, Xie H, Xin Z, Li Y, Chen L. Enhancing thermal conductivity of palmitic acid based phase change materials with carbon nanotubes as fillers. Sol Energy 2010;84(2):339–44.
[15] Ji P, Sun H, Zhong Y, Feng W. Improvement of the thermal conductivity of a phase change material by the functionalized carbon nanotubes. Chem Eng Sci 2012;81:140–5.
[16] Li T, Lee J-H, Wang R, Kang YT. Heat transfer characteristics of phase change nanocomposite materials for thermal energy storage application. Int J Heat Mass Tran 2014;75:1–11.
[17] Lohrasbi S, Sheikholeslami M, Ganji DD. Discharging process expedition of NEPCM in fin-assisted latent heat thermal energy storage system. J Mol Liq 2016;221:833–41.
[18] Sheikholeslami M, Mahian O. Enhancement of PCM solidification using inorganic nanoparticles and an external magnetic field with application in energy storage systems. J Clean Prod 2019;215:963–77.
[19] Lin SC, Al-Kayiem HH. Evaluation of copper nanoparticles – paraffin wax compositions for solar thermal energy storage. Sol Energy 2016;132:267–78.
[20] Barhemmati-Rajab N, Zhao W. Investigation into boron nitride nanoparticle effects on thermal properties of calcium chloride hexahydrate (CaCl2·6H2O) as a phase change material. MRS Communications 2018;8(4):1439–44.
[21] Tauseef ur R, Ali HM, Janjua MM, Sajjad U, Yan W-M. A critical review on heat transfer augmentation of phase change materials embedded with porous materials/foams. Int J Heat Mass Tran 2019;135:649–73.
[22] Xiao X, Zhang P, Li M. Preparation and thermal characterization of paraffin/metal foam composite phase change material. Appl Energy 2013;112:1357–66.
[23] Mancin S, Diani A, Doretti L, Hooman K, Rossetto L. Experimental analysis of phase change phenomenon of paraffin waxes embedded in copper foams. Int J Therm Sci 2015;90:79–89.
[24] Mehryan SAM, Heidarshenas MH, Hajjar A, Ghalambaz M. Numerical study of melting-process of a non-Newtonian fluid inside a metal foam. Alexandria Engineering Journal 2020;59(1):191–207.
[25] Ghalambaz M, Zhang J. Conjugate solid-liquid phase change heat transfer in heatsink filled with phase change material-metal foam. Int J Heat Mass Tran 2020;146:118832.
[26] Mahdi JM, Lohrasbi S, Nsofor EC. Hybrid heat transfer enhancement for latent-heat thermal energy storage systems: a review. Int J Heat Mass Tran 2019;137:630–49.
[27] Sardari PT, Mohammed HI, Giddings D, walker GS, Gillott M, Grant D. Numerical study of a multiple-segment metal foam-PCM latent heat storage

unit: effect of porosity, pore density and location of heat source. Energy 2019;189:116108.

[28] Xie YQ, Song J, Chi PT, Yu JZ. Performance enhancement of phase change thermal energy storage unit using fin and copper foam. Conference Performance enhancement of phase change thermal energy storage unit using fin and copper foam, vol. vol. 260. Trans Tech Publ, p. 137-141.

[29] Zhang C, Fan Y, Yu M, Zhang X, Zhao Y. Performance evaluation and analysis of a vertical heat pipe latent thermal energy storage system with fins-copper foam combination. Appl Therm Eng 2020;165:114541.

[30] Feng S, Shi M, Li Y, Lu TJ. Pore-scale and volume-averaged numerical simulations of melting phase change heat transfer in finned metal foam. Int J Heat Mass Tran 2015;90:838—47.

[31] Srivatsa PVSS, Baby R, Balaji C. Numerical investigation of PCM based heat sinks with embedded metal foam/crossed plate fins. Numer Heat Tran, Part A: Applications 2014;66(10):1131—53.

[32] Zhang C, Yu M, Fan Y, Zhang X, Zhao Y, Qiu L. Numerical study on heat transfer enhancement of PCM using three combined methods based on heat pipe. Energy 2020;195:116809.

[33] Abdulateef AM, Abdulateef J, Al-Abidi AA, Sopian K, Mat S, Mahdi MS. A combination of fins-nanoparticle for enhancing the discharging of phase-change material used for liquid desiccant air conditioning unite. Journal of Energy Storage 2019;24:100784.

[34] Xiong Q, Tlili I, Dara RN, Shafee A, Nguyen-Thoi T, Rebey A, et al. Energy storage simulation involving NEPCM solidification in appearance of fins. Phys Stat Mech Appl 2020;544:123566.

[35] Mahdi JM, Nsofor EC. Melting enhancement in triplex-tube latent thermal energy storage system using nanoparticles-fins combination. Int J Heat Mass Tran 2017;109:417—27.

[36] Li Z, Shahsavar A, Al-Rashed AAAA, Talebizadehsardari P. Effect of porous medium and nanoparticles presences in a counter-current triple-tube composite porous/nano-PCM system. Appl Therm Eng 2020;167:114777.

[37] Hossain R, Mahmud S, Dutta A, Pop I. Energy storage system based on nanoparticle-enhanced phase change material inside porous medium. Int J Therm Sci 2015;91:49—58.

[38] Tasnim SH, Hossain R, Mahmud S, Dutta A. Convection effect on the melting process of nano-PCM inside porous enclosure. Int J Heat Mass Tran 2015;85:206—20.

[39] Buonomo B, Ercole D, Manca O, Nardini S. Nanoparticles and metal foam in thermal control and storage by phase change materials. In: Handbook of thermal science and engineering. Cham: Springer International Publishing; 2018. p. 859—83.

[40] Mahdi JM, Nsofor EC. Solidification enhancement in a triplex-tube latent heat energy storage system using nanoparticles-metal foam combination. Energy 2017;126:501—12.

[41] Hussanan A, Salleh MZ, Khan I, Shafie S. Convection heat transfer in micropolar nanofluids with oxide nanoparticles in water, kerosene and engine oil. J Mol Liq 2017;229:482—8.

[42] Kant K, Shukla A, Sharma A, Biwole PH. Heat transfer study of phase change materials with graphene nano particle for thermal energy storage. Sol Energy 2017;146:453—63.

[43] Nield DA, Bejan A. Convection in porous media. Springer Science & Business Media; 2006.

[44] Buongiorno J. Convective transport in nanofluids. J Heat Tran 2006;128(3):240—50.

[45] Sheikholeslami M, Shamlooei M, Moradi R. Fe3O4-Ethylene glycol nanofluid forced convection inside a porous enclosure in existence of Coulomb force. J Mol Liq 2018;249:429—37.

[46] Mahdi JM, Nsofor EC. Melting enhancement in triplex-tube latent heat energy storage system using nanoparticles-metal foam combination. Appl Energy 2017;191:22—34.

[47] Shahsavar A, Al-Rashed AAAA, Entezari S, Sardari PT. Melting and solidification characteristics of a double-pipe latent heat storage system with sinusoidal wavy channels embedded in a porous medium. Energy 2019;171:751—69.

[48] Ranut P. On the effective thermal conductivity of aluminum metal foams: review and improvement of the available empirical and analytical models. Appl Therm Eng 2016;101:496—524.

[49] Mesalhy O, Lafdi K, Elgafy A, Bowman K. Numerical study for enhancing the thermal conductivity of phase change material (PCM) storage using high thermal conductivity porous matrix. Energy Convers Manag 2005;46(6):847—67.

[50] Zheng H, Wang C, Liu Q, Tian Z, Fan X. Thermal performance of copper foam/paraffin composite phase change material. Energy Convers Manag 2018;157:372—81.

[51] Reddy JN, Gartling DK. The finite element method in heat transfer and fluid dynamics. CRC press; 2010.

[52] Zienkiewicz OC, Taylor RL, Nithiarasu P. The finite element method for fluid dynamics. Elsevier; 2015.

[53] De Los Reyes JC, González Andrade S. A combined BDF-semismooth Newton approach for time-dependent Bingham flow. Numer Methods Part Differ Equ 2012;28(3):834—60.

[54] Schenk O, Gärtner K. Solving unsymmetric sparse systems of linear equations with PARDISO. Future Generat Comput Syst 2004;20(3):475—87.

[55] Wriggers P. Nonlinear finite element methods. Springer Science & Business Media; 2008.

[56] Verbosio F, De Coninck A, Kourounis D, Schenk O. Enhancing the scalability of selected inversion factorization algorithms in genomic prediction. Journal of computational science 2017;22:99—108.

[57] Kumar L, Manjunath BS, Patel RJ, Markandeya SG, Agrawal RG, Agrawal A, et al. Experimental investigations on melting of lead in a cuboid with constant heat flux boundary condition using thermal neutron radiography. Int J Therm Sci 2012;61:15—27.

[58] Bertrand O, Binet B, Combeau H, Couturier S, Delannoy Y, Gobin D, et al. Melting driven by natural convection A comparison exercise: first results. Int J Therm Sci 1999;38(1):5—26.

[59] Kuehn TH, Goldstein RJ. An experimental and theoretical study of natural convection in the annulus between horizontal concentric cylinders. J Fluid Mech 1976;74:695.

[60] Ren Q. Enhancement of nanoparticle-phase change material melting performance using a sinusoidal heat pipe. Energy Convers Manag 2019;180:784—95.

[61] Brinkman HC. The Viscosity of Concentrated Suspensions and Solutions. J Chem Phys 1952;20(4):571—81.

[62] Kakaç S, Pramuanjaroenkij A. Review of convective heat transfer enhancement with nanofluids. Int J Heat Mass Tran 2009;52(13):3187—96.

[63] Ma Z, Lin W, Sohel MI. Nano-enhanced phase change materials for improved building performance. Renew Sustain Energy Rev 2016;58:1256—68.

[64] Feng Y, Li H, Li L, Bu L, Wang T. Numerical investigation on the melting of nanoparticle-enhanced phase change materials (NEPCM) in a bottom-heated rectangular cavity using lattice Boltzmann method. Int J Heat Mass Tran 2015;81:415—25.

[65] Yang L, Huang J-n, Zhou F. Thermophysical properties and applications of nano-enhanced PCMs: An update review. Energy Convers Manag 2020;214:112876.

[66] Ghahremannezhad A, Xu H, Reza Salimpour M, Wang P, Vafai K. Thermal Performance Analysis of Phase Change Materials (PCMs) Embedded in Gradient Porous Metal Foams. Appl Therm Eng 2020:115731.

[67] Xu Y, Ren Q, Zheng Z-J, He Y-L. Evaluation and optimization of melting performance for a latent heat thermal energy storage unit partially filled with porous media. Appl Energy 2017;193:84—95.

[68] Joshi V, Rathod MK. Thermal transport augmentation in latent heat thermal energy storage system by partially filled metal foam: A novel configuration. J Energy Storage 2019;22:270—82.

[69] Joshi V, Rathod MK. Thermal performance augmentation of metal foam infused phase change material using a partial filling strategy: An evaluation for fill height ratio and porosity. Appl Energy 2019;253:113621.

[70] Ma Z, Lin W, Sohel MI. Nano-enhanced phase change materials for improved building performance. Renew Sustain Energy Rev 2016;58:1256—68.

[71] Kant K, Shukla A, Sharma A, Biwole PH. Heat transfer study of phase change materials with graphene nano particle for thermal energy storage. Sol Energy 2017;146:453—63.